Coordination of cell cycle and morphogenesis during organ formation

Jeffrey Matthew, Vishakha Vishwakarma, Thao Phuong Le, Ryan A. Agsunod, and SeYeon Chung*

Department of Biological Sciences, Louisiana State University, Baton Rouge, LA 70803, USA
*Author for correspondence: seyeonchung@lsu.edu

Keywords: *Drosophila*, salivary gland, Huckebein, endoreplication, endocycle, apoptosis, epithelial tube formation

Running title: Hkb regulates endoreplication during *Drosophila* salivary gland morphogenesis

Abstract

Organ formation requires precise regulation of cell cycle and morphogenetic events. Using the *Drosophila* embryonic salivary gland (SG) as a model, we uncover the role of the SP1/KLF transcription factor Huckebein (Hkb) in coordinating cell cycle regulation and morphogenesis. The *hkb* mutant SG exhibits defects in invagination positioning and organ size due to abnormal death of SG cells. Normal SG development involves distal-to-proximal progression of endoreplication (endocycle), whereas *hkb* mutant SG cells undergo abnormal cell division, leading to cell death. Hkb represses the expression of key cell cycle and pro-apoptotic genes in the SG. Knockdown of *cyclin E* or *cyclin-dependent kinase 1,* or overexpression of *fizzy-related* rescues most of the morphogenetic defects observed in the *hkb* mutant SG. These results indicate that Hkb plays a critical role in controlling endoreplication by regulating the transcription of key cell cycle effectors to ensure proper organ formation.

Introduction

The formation of tubular organs, such as the lungs and kidneys, begins with the folding of flat epithelial tissues into functional three-dimensional (3D) tubular structures. In humans, errors in tube formation can result in congenital defects such as spina bifida and lung hypoplasia (Wilde et al., 2014). Studies in both vertebrates and invertebrates have revealed key morphogenetic mechanisms underlying epithelial tube formation during development (Andrew and Ewald, 2010; Chung et al., 2014; Herriges and Morrisey, 2014; Girdler and Röper, 2014; Nikolopoulou et al., 2017; Spina and Cowin, 2021; Pradhan et al., 2023). While proper cell shape changes and cell rearrangement are critical, precise regulation of cell division and cell death is also essential for tissue morphogenesis (Huh et al., 2004; Mao et al., 2013; LeGoff and Lecuit, 2015; Godard and Heisenberg, 2019). Notably, the interplay between cell division and cell death provides a homeostatic control system necessary for proper organ formation. Perturbations at any stage of the cell cycle can have detrimental effects on cell viability, leading to cell death, and activation of apoptosis can trigger compensatory proliferation in surrounding cells (Ryoo et al., 2004). In addition to their role in establishing and maintaining the correct number of cells in tissues and organs, cell division and cell death generate biophysical forces through actomyosin reorganization that help shape the final tissue morphology. For example, during *Drosophila* tracheal invagination, mitotic cell rounding drives the internalization of the tracheal primordium (Kondo and Hayashi, 2013). During dorsal closure and leg folding in *Drosophila* (Toyama et al., 2008; Monier et al., 2015) and neural closure in mammals (Massa et al., 2009; Yamaguchi et al., 2011), apoptotic cells generate forces at both local and tissue scales that affect tissue remodeling. Therefore, to fully understand the mechanisms of organ formation, it is critical to know how the cell cycle, cell death, and morphogenesis are coordinated during epithelial tube formation.

The *Drosophila* embryonic salivary gland (SG) is a premier model for studying the mechanisms of tube formation from a flat epithelial sheet (Chung et al., 2014; Sidor and Röper, 2016). The *Drosophila* embryo contains two SGs, each consisting of 140-150 cells, which initially reside on the embryo surface and invaginate to form single-layered, elongated tubes (Fig. 1A). Once SG cells are specified, they do not divide or die. Cell death is actively inhibited during SG morphogenesis. The SG-upregulated transcription factors Fork head (Fkh), Senseless, and Sage inhibit apoptosis by downregulating proapoptotic genes, such as *head involution defective* (*hid*)

70 and *reaper* (*rpr*) (Myat and Andrew, 2000a; Chandrasekaran and Beckendorf, 2003; Fox et al.,
71 2013). Instead of cell division, SG cells undergo endoreplication (endocycle), a variant of the
72 cell cycle that involves DNA replication without subsequent cell division forming polyploid
73 cells, upon invagination at stage 11 (Follette et al., 1998). SG cells that have completed one
74 round of endoreplication arrest the cell cycle in G2 until the larval stage (Smith and Orr-Weaver,
75 1991; Chandrasekaran and Beckendorf, 2005). Endoreplication, which is more common in
76 invertebrates and plants, was thought to be a rare cell cycle variation in mammals. However,
77 recent studies have revealed endoreplication in various mammalian tissues, including humans,
78 and endoreplication is emerging as a potential developmental timer (Gandarillas et al., 2018).
79 Like the conventional cell cycle, endoreplication is regulated by key cell cycle genes such as
80 cyclins and cyclin-dependent kinases (CDKs). In *Drosophila* embryogenesis, re-entry into S
81 phase during endoreplication is regulated by the cyclin E-Cdk2 complex through the E2F
82 proteins (Duronio et al., 1995; Follette et al., 1998). Because SG morphogenesis occurs in the
83 absence of cell division and cell death, studies of SG morphogenesis have primarily focused on
84 the mechanisms underlying cell shape changes, cell intercalation, and collective cell migration
85 (Pirraglia et al., 2010; Xu et al., 2011; Röper, 2012; Ismat et al., 2013; Booth et al., 2014; Chung
86 et al., 2014; Chung et al., 2017; Sanchez-Corrales et al., 2018; Sanchez-Corrales et al., 2021; Le
87 and Chung, 2021; Vishwakarma et al., 2022). Little is known about the potential impact of
88 regulating endoreplication and cell death during SG morphogenesis.

89 Invagination is the first step in SG morphogenesis that is critical for organ architecture, and
90 studies in recent years have revealed key underlying molecular and cellular mechanisms (Chung
91 et al., 2017; Sanchez-Corrales et al., 2018; Sidor et al., 2020; Sanchez-Corrales et al., 2021; Le
92 and Chung, 2021; Vishwakarma et al., 2022). SG invagination occurs in a stereotypical manner,
93 with two predominant cell behaviors occurring in distinct spatial domains within the placode
94 relative to the invagination pit forming in the dorsal/posterior region: clustered apical
95 constriction near the pit (Fig. 1A) and cell intercalation far from the pit. Two early-expressed
96 SG-upregulated transcription factors, Fkh and Huckebein (Hkb), play critical roles in SG
97 invagination. Fkh, a winged-helix transcription factor that regulates more than two-thirds of the
98 known SG genes, is essential for SG invagination; SG cells fail to invaginate in *fkh* mutants in
99 which apoptosis is inhibited (Myat and Andrew, 2000a; Maruyama et al., 2011). Hkb, an

100 SP1/KLF transcription factor, is crucial for invagination positioning; SG cells invaginate in the
101 central region of the placode in *hkb* mutants (Myat and Andrew, 2000b). A recent study
102 proposed that the early patterning of Fkh and Hkb and their downstream effectors ensures
103 positionally fixed cell behaviors with respect to invagination position (Sanchez-Corrales et al.,
104 2021). For example, a key downstream target of Fkh, Folded gastrulation (Fog), signals through
105 its G protein-coupled receptor to activate Rho kinase and myosin to regulate apical constriction
106 in the dorsal/posterior region of the SG placode (Chung et al., 2017; Vishwakarma et al., 2022).
107 Despite the intriguing phenotype of *hkb* mutants, the mechanism of how Hkb regulates SG
108 invagination positioning remains largely unknown. Only two potential downstream targets of
109 Hkb involved in SG formation have been identified: *crumbs* (*crb*), encoding a key apical
110 membrane protein, and *klarsicht* (*klar*), encoding a Nesprin family protein that mediates dynein-
111 dependent organelle trafficking (Myat and Andrew, 2002). To fully understand the mechanism of
112 how Hkb regulates invagination position, it is critical to reveal the precise cellular mechanisms
113 underlying the centered invagination phenotype and identify Hkb downstream targets regulating
114 the process.

115 In this study, we reveal the distal-to-proximal progression of endoreplication during SG
116 morphogenesis and show that Hkb plays a critical role in this process. Loss of *hkb* results in
117 abnormal cell division in the SG leading to cell death. Subsequently, abnormal cell death leads to
118 malposition of the SG invagination and formation of a smaller organ. Using modENCODE Hkb
119 ChIP-Seq targets and genetic interaction analyses, we show that Hkb represses the transcription
120 of key cell cycle genes in the SG to control cell cycle progression and ensure cell survival and
121 proper SG morphogenesis.

Materials and Methods

Fly stocks and genetics

The fly stocks used in this study are listed in Table S1. All the crosses were performed at 25°C, except for Hkb expression using fkh-Gal4 and UAS-Hkb for the rescue experiment, which was performed at 29°C for higher levels of transgene expression.

Generation of *hkb* mutant alleles

hkb mutant alleles were generated using CRISPR/Cas9. Using flyCRISPR Target Finder (http://targetfinder.flycrispr.neuro.brown.edu/), we identified two gRNAs, one in the first exon of the *hkb* transcript near the 5' end of the gene (gRNA3) and the other in the second zinc finger domain (gRNA1). Both gRNAs exhibited maximum stringency, with zero predicted off-target effects. The sense and antisense oligos for each gRNA sequence were annealed and cloned into the pU6-BsaI-gRNA vector (a kind gift from Jean-Paul Vincent; (Baena-Lopez et al., 2013)) via the BsaI restriction site. The constructs were confirmed by Sanger sequencing before injection. The following sense and antisense oligonucleotides were used for creating null (gRNA3) and hypomorphic (gRNA1) alleles (PAM sequences underlined and linkers in small characters).

gRNA1 sequence: 5'-ACGCGTCAGTTCCTCATTGC<u>GGG</u>-3'
sense oligo, 5'-tccACGCGTCAGTTCCTCATTGC-3'
antisense oligo, 5'-aaacGCAATGAGGAACTGACGCGT-3'

gRNA3 sequence: 5'-AAAGTCGCGAGTAGGTTTGC<u>GGG</u>-3'
sense oligo, 5'-tccAAAGTCGCGAGTAGGTTTGC-3'
antisense oligo, 5'-aaacGCAAACCTACTCGCGACTTT-3'

The pU6-gRNA1/3 constructs (500 ng/µl per gRNA) were sent to GenetiVision for injections. GenetiVision performed injection into nos-Cas9 embryos. Individual G0 adults were crossed to w; TM3, Sb/TM6B, Tb flies. Five offspring (F1) for each cross were independently crossed to w; TM3, Sb/TM6B, Tb to generate independent stocks. The DNA fragment encompassing the gRNA sites was PCR amplified using a single adult fly of each stock, and indels at the

152 corresponding gRNA site were confirmed by Sanger sequencing. The following primers were
153 used for both PCR and sequencing.
154
155 Hkb_FWD, 5'-AGATTGGGTTTGGTGAGTGC-3'
156 Hkb_REV, 5'-TCGCACATCCTCAGACAGAC-3'

157 The predicted protein sequences and details of indels for each allele were described in Sup. Fig.
158 S1.

159

160 **Generation of Hkb-mCherry fusion protein lines**

161 To create the functional Hkb-mCh fusion protein line, mCherry was inserted into six amino acids
162 upstream from the C-terminal end of the Hkb protein in frame with the Hkb protein using the
163 homology-directed repair of the CRISPR/Cas9 technique. The gRNA near the C-terminal end of
164 the protein was chosen (Hkb_C_gRNA3, 5'-CCCATGTACTCATACCTTTATGG-3') using the
165 flyCRISPR Target Finder (http://targetfinder.flycrispr.neuro.brown.edu/). Genomic DNA regions
166 that flank the gRNA locus were amplified using the WT genomic DNA for the left and right
167 homology arms (HAL (1066 bp) and HAR (1408 bp)). DNA fragments for the open reading
168 frame of the mCherry protein and the backbone plasmid were amplified using the pENTR R4-
169 mCherry-R3 plasmid (Addgene #32311) as a template. The donor DNA construct containing
170 both homology arms (pENTR-HAL-mCherry-HAR; 5853 bp) was created using the NEBuilder
171 HiFi DNA Assembly Master Mix (NEB #E2621). The following primers were used for
172 amplifying each DNA fragment.
173
174 mCh_FWD, 5'-CCATCTTCGTGCCCATGTACATGGTGAGCAAGGGCGAG-3'
175 mCh_REV, 5'-CTTGTACAGCTCGTCCATGC-3'
176 Backbone_FWD, 5'-CTATGCCGTCTCCATTCGATACAACTTTGTATAATAAAGTTGAAC-
177 3'
178 Backbone_REV, 5'-GTTGGCCAACTTTGTATAG-3'
179 HAL_FWD, 5'-TCTATACAAAGTTGGCCAACAGATCTCGCAGCACACAC-3'
180 HAL_REV, 5'-GTACATGGGCACGAAGATG-3'
181 HAR_FWD, 5'-GCATGGACGAGCTGTACAAGTCATACCTTTATGGCTACTGAG-3'

182 HAR_REV, 5'-ATCGAATGGAGACGGCATAG-3'
183
184 The same strategy was used to create the Hkb^{mut}-mCh knock-in line. The mCh tag was inserted
185 into the N-terminal region of Hkb, using gRNA3, the same gRNA used to create null mutant
186 alleles. A stop codon was added to the C-terminal end of the mCh tag. Genomic DNA regions
187 that flank the gRNA locus were amplified using the WT genomic DNA for the left and right
188 homology arms (HAL (1130 bp) and HAR (1153 bp)). The following primers were used for
189 amplifying each DNA fragment.
190
191 mCh_FWD, 5'- CCCGCAAATGGTGAGCAAGGGC -3'
192 mCh_REV, 5'- GCGAGTAGGTCTACTTGTACAGCT-3'
193 Backbone_FWD, 5'-
194 AAATATTGAGATACAACTTTGTATAATAAAGTTGAACGAGAAACGTAAAA -3'
195 Backbone_REV, 5'- TGGCTGCAGTTGGCCAACTTTGTATAGAAAAGTTGAAC -3'
196 HAL_FWD, 5'- GGCCAACTGCAGCCAGAATCGCG -3'
197 HAL_REV, 5'- CTCACCATTTGCGGGGGATG -3'
198 HAR_FWD, 5'- TACAAGTAGACCTACTCGCGACTTTTCC-3'
199 HAR_REV, 5'-
200 TATACAAAGTTGTATCTCAATATTTGCATATATCGTCGAGGTCCAAAGA -3'
201
202 The pENTR-HAL-mCherry-HAR constructs (500 ng/µl per gRNA) were sent to GenetiVision
203 for injections. GenetiVision performed injection into nos-Cas9 embryos. Individual G0 adults
204 were crossed to w; TM3, Sb/TM6B, Tb flies. Five offspring (F1) from each of the surviving
205 crosses were independently crossed to w; TM3, Sb/TM6B, Tb to generate independent stocks.
206 Fluorescent signals for mCherry in Hkb^{WT}-mCh and Hkb^{mut}-mCh transgenic lines were confirmed
207 by immunostaining using the antibody against mCherry.
208

209 **Immunostaining and imaging**

210 *Drosophila* embryos were collected on grape juice agar plates at 25°C. Embryos were
211 dechorionated by incubating in 50% bleach for 3 minutes. For most samples, embryos were fixed

212 in formaldehyde-saturated heptane for 40 minutes and devitellinized using 80% ethanol.
213 Following this, the embryos were stained with primary and secondary antibodies in PBSTB (1X
214 PBS, 0.2% bovine serum albumin, and 0.1% Triton X-100). For phalloidin and sqh-GFP signals,
215 embryos were hand-devitellinized and stained with primary and secondary antibodies in PBTr
216 (1X PBS and 0.1% Triton X-100). The antibodies used in this study and their respective dilutions
217 are listed in Table S2. After staining, embryos were mounted in Aqua-Poly/Mount (Polysciences,
218 Inc.) and imaged with Leica SP8 confocal microscope using 63x, NA 1.4 and 40x, NA 1.3
219 objectives. For horseradish peroxidase (HRP) staining, the VECTASTAIN® ABC-HRP Kit,
220 Peroxidase (PK-4000; Vector Laboratories) was used with biotin-conjugated secondary
221 antibodies. Whole embryo HRP images were acquired with a Leica DM2500 microscope using a
222 20×, 0.8 NA objective.

223

224 **Cell segmentation, apical area quantification, and scatter plots**

225 SGs in early (pre-invagination; invagination depth, 0 μm) and late (during invagination;
226 invagination depth, 5-10 μm) stage 11 of embryos were used. Confocal images of the SG were
227 obtained from embryos immunostained for the Ecad (adherens junctions) and CrebA (SG cell
228 nuclei) and used for cell segmentation. A maximum intensity projection was generated using the
229 LasX program from three apical z-sections of confocal images of SG cells encompassing the
230 adherens junction. Using the maximum intensity projection, cells were segmented using Ecad
231 signals as a marker for each cell boundary using Imaris software (Andor). The apical area was
232 calculated using Imaris and individual cells were color-coded based on the size of their apical
233 areas. The frequency distribution of the apical area of the cells was analyzed using GraphPad
234 Prism with the data exported from Imaris. Since the output data from Imaris for the apical area
235 quantification is a sum of the area of both sides of the cell layer, we further divided the values by
236 2 to obtain the apical area of SG cells.

237 Scatter plots were generated using the X and Y coordinates for each SG cell, which were
238 determined with respect to the A/P and D/V axes of the tissue using Imaris. The cell at the center
239 of the SG placode was used as the origin point (X=0, Y=0).

240

241 **Quantification of SG cell numbers**

242 Confocal microscopy stacks for SGs with SG-specific nuclear markers (CrebA or Sage) were
243 used for early stage 11 (pre-invagination) and stage 15+ embryos. Three dimensional (3D)-
244 reconstructed images were generated using Imaris. The number of nuclei for each 3D-
245 reconstructed SG was counted using cell ID numbers.

246

247 **Quantification of SG lumen length and apical area of individual SG cells at stage 15**

248 SG lumen length at stage 15 was measured for the secretory portion of the gland based on CrebA
249 signals, which are exclusively expressed in the secretory cells at this stage. Confocal images
250 immunolabeled with markers for Ecad and CrebA for stage 15 SGs were used. 8-12 z-section
251 images of the SG were merged to obtain a maximum projection image clearly showing half of
252 the SG lumen and its apical surface. Segmentation of SG cells and quantification of apical areas
253 of individual cells were performed using Imaris as described for segmentation of SG cells at
254 stage 11.

255 For the lumen length quantification, maximum intensity projection images were imported into
256 the ImageJ software (Fiji). The length of the SG lumen was measured along the line following
257 the midpoint of the secretory portion of the tube.

258

259 **Quantification of SG phenotypes at embryonic stages 12 and 15+**

260 After performing HRP staining with CrebA, the SGs were manually categorized based on their
261 phenotypes. At stage 12, WT SGs turn and migrate towards the posterior of the embryo after
262 reaching the visceral mesoderm. SGs showing such normal behavior were categorized as
263 "normal", while those SGs that reached the visceral mesoderm and migrated slightly were
264 categorized as "turned but short", and those SGs that reached the visceral mesoderm but did not
265 migrate posteriorly were categorized as "not turned".

266 For stage 15+ embryos, SGs that were comparable in shape, size, and position to WT SGs were
267 categorized as "normal"; SGs that had a rounded/ball-like morphology were categorized as "very
268 short/rounded"; SGs that were slightly elongated but not as long as WT SGs and mislocalized
269 anteriorly were categorized as "intermediate, mislocalized"; SGs that were slightly elongated but
270 in the normal position were categorized as "intermediate, normal position". SGs that were as
271 long as WT but mislocalized anteriorly were categorized as "long, mislocalized".

272

273 **Analysis of modENCODE Hkb ChIP-Seq targets**

274 The dataset was downloaded from the ENCODE Portal (https://www.encodeproject.org/). Total
275 1268 ChIP-Seq targets were analyzed using Database for Annotation, Visualization and
276 Integrated Discovery (DAVID; Dennis et al., 2003).

277

278 **EdU labeling**

279 To visualize SG cells in the S phase of the cell cycle or undergoing endoreplication,
280 dechorionated embryos were incubated in n-octane (Thermo Scientific Chemicals: 325950010)
281 for 3 minutes to permeabilize the vitelline membrane. Embryos were then washed 5 times in 1x
282 PBS in a microcentrifuge tube before being pulsed with 100µM EdU (Thermofisher: C10637)
283 for 30 minutes. Following EdU labeling, embryos were washed 5 times for 5 minutes each in
284 PBSTB and incubated with azide-conjugated Alexa Fluor 488 for 30 minutes at room
285 temperature. Embryos were further stained with CrebA and Crumbs antibodies to mark SG cell
286 nuclei and apical cell boundaries, respectively.

287

288 **Fluorescence in situ hybridization**

289 Dechorionated *Drosophila* embryos were fixed in paraformaldehyde-heptane solution for 30
290 min, followed by devitellinization using methanol. Freshly fixed embryos were then labeled with
291 digoxigenin (DIG)-labeled antisense probes following the standard procedure described in Knirr
292 et al. (1999). After rehydration and post-fixation in 10% formaldehyde, embryos were pre-

293 hybridized for 1 hour at 55°C. mRNA probes were added to the embryos which were then
294 incubated for 16 hours at 55°C. DIG present on the synthesized mRNA probes was subsequently
295 labeled with anti-DIG primary antibody (Enzo; ENZ-ABS302-0001; 1:1,000) and biotin-
296 conjugated secondary antibody (Invitrogen; 1:500). To detect fluorescent signals, embryos were
297 incubated with AB solution (PK-6100, Vectastain Elite ABC kit) followed by the tyramide signal
298 amplification reaction (Cy3 fluorescent dye in amplification diluent; 1:50) (Perkin Elmer Life
299 Sciences, NEL753001kt). To mark the SG and the apical membrane, the embryos were
300 immunolabeled with antibodies for CrebA (SG nuclei) and Crb (apical membrane).

301 Primer sequences used for mRNA probe synthesis in this study are listed below.

Gene name	Primer sequence	Probe size
Cyclin A (*CycA*)	Forward: 5'-TAAACCACGAACCGCTGAAC-3' Reverse: 5'-CATGGTGCGCTCTTTCCTAC-3'	443 bp
Cyclin E (*CycE*)	Forward: 5'-TGGACTGGTTGATCGAGGTC-3' Reverse: 5'-TCAAAGCCAGAGAATTGCGG-3'	424 bp
E2f1	Forward: 5'-CAGTCCGCAAAAATGTGAAA-3' Reverse: 5'-TATCACACGCAACCACAACA-3'	500 bp
fizzy-related (*fzr*)	Forward: 5'-ACCCCACAGCAGCAATAGAT-3' Reverse: 5'-TTCGGGGGTATGAGTGTTTC-3'	417 bp
reaper (*rpr*)	Forward: 5'-CGAAAGAAAAGTGTGTGCGC-3' Reverse: 5'-GTTGTGGCTCTGTGTCCTTG-3'	483 bp
string (*stg*)	Forward: 5'-GCGACTGATGCTGTAGGTTG-3' Reverse: 5'-AGGGGTCTGATTTCGGGATC-3'	407 bp

302

303 **Quantification of *in situ* hybridization signals**

304 Stage 11 *hkb* mutant and WT SGs were used. A maximum intensity projection was generated
305 using two z-sections of confocal images of SG cells. Z-sections were obtained from the same
306 depth in all instances. Snapshots of these sections were imported into Fiji (NIH), and SG *mRNA*
307 expression levels were measured by obtaining the mean gray value of the fluorescence intensity
308 across the SG placode. SG placode-specific measurements were performed using SG-expressed
309 CrebA signals. For each *mRNA* quantification, background subtraction was done using 10-15
310 cells in the epidermis in the lateral ectoderm region of parasegment 2 near the SG. Statistical
311 analysis was performed using GraphPad Prism.

312

313

314 **Results**

315 **Creation of the molecularly defined *hkb* mutant alleles and fluorescent knock-in lines**

316 To fully characterize the role of Hkb during SG morphogenesis, we generated two null (hkb^{351},
317 hkb^{391}) and two hypomorphic alleles (hkb^{121}, hkb^{131}) using CRISPR/Cas9 (Figure 1B; Details of
318 indels and expected protein sequences were described in Figure 1-figure supplement 1). All
319 alleles were embryonic lethal in homozygous embryos and transheterozygotes with a deficiency
320 line deleting the *hkb* locus, suggesting that all three zinc-finger (ZnF) domains are required for
321 embryonic development and survival. Immunostaining with CrebA, a nuclear marker for
322 secretory cells of the SG, and E-Cadherin (Ecad), an adherens junction marker, showed that
323 wild-type (WT) embryos exhibited SG invagination in the dorsal-posterior region of the placode
324 (Figure 1C). However, new *hkb* alleles exhibited a broad, central SG invagination phenotype
325 (Figure 1D, E), similar to previous studies with an EMS allele hkb^{2} and a P-element excision
326 allele hkb^{A321R1} (Weigel et al., 1990; Gaul and Weigel, 1990; Myat and Andrew, 2002; De laco et
327 al., 2005; Sanchez-Corrales et al., 2021). hkb^{121} also exhibited the centered invagination
328 phenotype, albeit with only 50% penetrance (Figure 1D; N=20), indicating that all three ZnF
329 domains are required for the positioning of the SG invagination.

330 We also generated two mCherry-tagged transgenic lines, Hkb^{WT}-mCh (a functional fusion
331 protein line) and Hkb^{mut}-mCh (a mutant knock-in line) using CRISPR-mediated homology-
332 directed repair (Figure 1B). The Hkb^{WT}-mCh line exhibited nuclear mCh signals in several
333 tissues known to express Hkb, including the anterior and posterior termini of the early embryo,
334 SGs, and a subset of neuroblasts (Figure 1F, F' and Figure 1-figure supplement 2). In the SG,
335 strong Hkb^{WT}-mCh signals were detected at stages 10 and 11, with higher levels in the posterior
336 region of the placode at stage 10 (Figure 1-figure supplement 2C-F''), consistent with a previous
337 study (Sanchez-Corrales et al., 2021). Weak Hkb^{WT}-mCh signals were present at stages 12 and
338 13 and not detected thereafter (Figure 1-figure supplement 2G-J''), consistent with the transient
339 expression of *hkb* transcripts in the SG (Myat and Andrew, 2002). Unlike the nuclear Hkb^{WT}-
340 mCh signals, Hkb^{mut}-mCh signals were distributed throughout the cell (Figure 1G, G' and Figure
341 1-figure supplement 2). In homozygous Hkb^{mut}-mCh and heterozygous Hkb^{mut}-mCh/+ embryos,

342 mCh signals persisted throughout the SG cell until stage 16, likely due to the loss of the Hkb
343 protein degradation elements/signals (Figure 1-figure supplement 2J-J'', T-T'').

344 To investigate the effect of *hkb* loss on SG cell behavior during invagination at stage 11, we
345 analyzed the distribution of SG cells undergoing apical constriction in WT and *hkb* mutants
346 using cell segmentation analysis (Figure 1H-K'and Figure 1-figure supplement 3). Before
347 invagination, WT SG cells with small apical areas clustered in the dorsal-posterior region of the
348 placode, whereas *hkb* mutants exhibited a scattered distribution (Figure 1-figure supplement 3D-
349 F'). As invagination progressed, more cells with small apical areas were observed near the
350 invagination pit in WT, whereas these cells were distributed around the wide central pit in *hkb*
351 mutant SGs (Figure 1H-J'). This is consistent with a previous study using hkb^{2} (Sanchez-
352 Corrales et al., 2021), although we observed that only about 30% of the hkb^{2} embryos showed
353 the central SG invagination phenotype (N=11). The frequency distribution of cells based on their
354 apical areas showed a significantly lower percentage of SG cells with smaller apical areas in *hkb*
355 mutants compared to WT (Figure 1K, K' and Figure 1-figure supplement 3G, G'), indicating a
356 defect in apical constriction.

357 Using CrebA signals, we analyzed SG morphology in late-stage WT and homozygous *hkb*
358 mutant embryos, as well as *hkb* transheterozygous embryos over a deficiency line deleting the
359 *hkb* locus. At stage 12, while the WT SGs turned and migrated toward the posterior of the
360 embryo upon reaching the visceral mesoderm, SGs in *hkb* mutant embryos migrated only slightly
361 posteriorly (Figure 1L-N and Figure 1-figure supplement 4A-E). Consistent with the role of Hkb
362 in endoderm specification (Brönner et al., 1994), *hkb* mutant embryos showed defects in gut
363 morphology, as well as defects in head development and occasional defects in germ band
364 retraction (Figure 1L'-N' and Figure 1-figure supplement 4B'-E'), making it difficult to
365 determine their correct stage after stage 14. Stage 15+ embryos in *hkb* mutants formed small SGs
366 compared to stage 15 WT embryos (Figure 1L'-N' and Figure 1-figure supplement 4A-E'), as in
367 a previous study (Myat and Andrew, 2000b). We observed a range of SG lengths. More than
368 40% of stage 15+ *hkb* null embryos and transheterozygotes of null over a deficiency (hkb^{351},
369 hkb^{391}, and hkb^{351}/Df) exhibited very short and ball-like SGs (Figure 1N', O' and Figure 1-figure
370 supplement 4). In contrast, the majority of *hkb* hypomorphic mutants and transheterozygotes of
371 hypomorphs over a deficiency (hkb^{121}, hkb^{131}, and hkb^{121}/Df) and other *hkb* mutants (hkb^{A321R1},

372 *hkb*^{2}, and *hkb*^{A321R1}/*Df*) had intermediate SG tube lengths (Figure 1M', O' and Figure 1-figure
373 supplement 4), suggesting that these alleles have a residual function of *hkb*. Homozygous
374 Hkb^{mut}-mCh embryos exhibited the same range of phenotypes as *hkb* null mutants, confirming
375 that the mCh insertion disrupts Hkb function (Figure 1-figure supplement 2).

376 In all *hkb* mutant lines, one or both SGs frequently mislocalized anteriorly, toward the head
377 center region (Figure 1M', N' and Figure 1-figure supplement 4C'-H'). Using the salivary duct
378 marker Dead Ringer (Dri; (Gregory et al., 1996)) and Ecad, we found that the mispositioning of
379 the SG may be due in part to the defects of the duct, likely resulting from a combination of
380 reduced cell number, aberrant apical domain size, and defective cell intercalation of duct cells
381 (Figure 1-figure supplement 5A-K'). We also found a transient Hkb expression in the SG duct at
382 early stage 11 (Figure 1-figure supplement 5L-M'), suggesting a possible role of Hkb during SG
383 duct morphogenesis.

384 Together, we have generated molecularly defined null and hypomorphic alleles of *hkb* and
385 fluorescently tagged knock-in transgenic lines. Since the two null and two hypomorphic alleles
386 behaved similarly, we used *hkb*^{351} and *hkb*^{121} for further analyses.

387

388 **Hkb is required for SG cell survival to ensure proper organ size**

389 To determine the cellular mechanisms underlying the small SG phenotype in *hkb* mutant
390 embryos, we measured the SG lumen length and counted SG cells using Ecad and CrebA signals,
391 respectively. Compared to WT, *hkb* null mutants and transheterozygous *hkb* null over a
392 deficiency showed a significantly shorter SG lumen length, and *hkb* hypomorphic embryos
393 showed a milder effect (Figure 2A-D, G). Surprisingly, *hkb* null mutants also showed fewer SG
394 cells compared to WT, with a moderate reduction at stage 11 and a significant reduction at stage
395 15 (stage 15+ for *hkb* mutants) (Figure 2G', G''). The effect was milder in hypomorphic
396 embryos (Figure 2G', G''), indicating a correlation between the SG lumen length and the number
397 of cells.

398 To test whether *hkb* mutant SG cells undergo apoptosis, we labeled WT, *hkb* mutant, and Hkb^{WT}-
399 mCh and Hkb^{mut}-mCh embryos with an antibody against *Drosophila* cleaved death caspase-1
400 (DCP-1; (Sarkissian et al., 2014)). WT and Hkb^{WT}-mCh SG cells showed no DCP-1 signals
401 (Figure 2H, N), except for a single cell at the anterior boundary of the SG placode in some stage
402 11 embryos (Arrowhead in Figure 2H). In contrast, SGs in *hkb* mutants and Hkb^{mut}-mCh
403 embryos displayed significant DCP-1 signals at stages 11 and 12 (Figure 2I-K, O, P and Figure
404 2-figure supplement 1A-C'). DAPI staining revealed condensed and fragmented nuclei in some
405 SG cells in *hkb* mutants (Figure 2Q, Q'), a hallmark of pyknosis (Zamzami and Kroemer, 1999).
406 At stages 13 and 14, several fragmented cells positive for DCP-1 and mCh, and negative for
407 CrebA, were found near the SG in Hkb^{mut}-mCh embryos (Figure 2R-R''; Figure 2-figure
408 supplement 1D-E''). Similar DCP-1-positive cells were found near the SG in *hkb* null mutants,
409 fewer in *hkb* hypomorphs, and rarely in WT embryos (Figure 2-figure supplement 1F-H'). These
410 cells, lacking CrebA signals but exhibiting nuclear fragmentation and condensation, are likely
411 late-stage apoptotic SG cells. Dying cells were also observed in other parts of the Hkb^{mut}-mCh
412 embryos near mCh-expressing regions compared to Hkb^{WT}-mCh embryos (Figure 2-figure
413 supplement 1I-K''), as well as some *hkb* mutant SG duct cells (Figure 1-figure supplement 5E,
414 E'), which may be the cause of the decreased duct cell numbers. This suggests a role for Hkb in
415 cell survival in multiple cell types.

416 We next performed a rescue experiment. Consistent with a previous study (Myat and Andrew,
417 2002), overexpression of Hkb in SG secretory cells using the *fkh-Gal4* driver (Henderson and
418 Andrew, 2000) in the otherwise WT background had no overt effects on SG formation, except
419 for an expanded SG lumen at late stages. Overexpression of Hkb in the SG in *hkb* mutants almost
420 completely rescued the short SG phenotype of *hkb* mutants, resulting in elongated SGs that
421 resembled WT SGs (Figure 2F; Figure 2-figure supplement 2C, K), with a reduced number of
422 DCP-1-positive SG cells (Figure 2L, P), and restored lumen length and SG cell number to WT
423 levels (Figure 2E, G''). Additionally, blocking apoptosis in the *hkb* mutant SG by overexpressing
424 the baculoviral protein p35, a caspase inhibitor of apoptosis, reduced the number of DCP-1-
425 positive cells (Figure 2M, P) and rescued the shortened SG phenotype, with restored SG cell
426 number (Figure 2G''; Figure 2-figure supplement 2F, K). These data suggest that the small SG
427 size in *hkb* mutants is primarily caused by apoptosis of SG cells.

428

429 **Hkb is required for apical domain elongation**

430 A previous study showed that *hkb* regulates apical domain elongation by regulating the key
431 apical protein Crb and the endocytic pathway regulator Klar (Myat and Andrew, 2002).
432 Although our data showed that the reduced number of SG cells is the main reason for the small
433 gland size in *hkb* mutants, defects in apical domain elongation may also contribute to this
434 phenotype. Measuring the apical area of individual SG cells in stage 15 embryos revealed that
435 *hkb* mutant SG cells have smaller apical domain sizes than WT (Figure 2-figure supplement 3A-
436 E). Immunostaining with Rab11, a recycling endosome marker, revealed that while WT SGs
437 showed Rab11 signals near the apical domain, *hkb* mutant SGs displayed basally mislocalized
438 Rab11 signals (Figure 2-figure supplement 3F-G'). These data suggest that impaired apical
439 trafficking and defective apical membrane elongation also contribute to the small gland
440 phenotype in *hkb* mutants.

441

442 **Aberrant cell death causes centered SG invagination in *hkb* mutants**

443 Next, we tested invagination positioning. SG-specific expression of Hkb corrected the centered
444 invagination defect in *hkb* mutants (Figure 3A-C), indicating a tissue-autonomous role of Hkb in
445 SG invagination positioning. Interestingly, blocking apoptosis in the SG also rescued the
446 centered invagination phenotype in *hkb* mutants (Figure 3D). In these embryos, cells with small
447 apical areas were mainly distributed in the dorsal/posterior quadrant of the SG placode (Figure
448 3E-F'), as in WT (Figure 1H, H'). SG-specific Hkb overexpression partially rescued the apical
449 constriction defects, and although not statistically significant, blocking apoptosis also slightly
450 decreased the number of SG cells with small apical areas in *hkb* mutants (Figure 3G, G'). Since
451 apoptotic cells undergo apical constriction before being eliminated from the epithelial sheet
452 (Toyama et al., 2008; Slattum et al., 2009; Marinari et al., 2012), we hypothesized that some SG
453 cells with small apical areas in *hkb* mutants are apoptotic. In support of this, we observed DCP-
454 1-positive cells with reduced apical areas in *hkb* mutant SGs at stage 11 (Figure 3H). Among the
455 SG cells of lower 30% of apical areas, more than 40% were DCP-1-positive (N=29/72 cells in 5

456 SGs from different embryos). We did not detect a significant spatial bias in the distribution of
457 DCP-1-positive cells among the four quadrants of the SG placode in *hkb* null mutants, although
458 slightly more DCP-1-positive cells were observed in the posterior region in hypomorphs and
459 transheterozygotes of null over deficiency (Figure 3I-J). When we analyzed the SG placode in
460 three domains (inner, outer, and mid), we found that most DCP-1-positive cells were in the mid
461 domain, especially in the null and transheterozygous conditions (Figure 3J'). This suggests a
462 correlation between the distribution of dying cells in the mid domain and the widened central
463 invagination pit observed in *hkb* mutants.

464 During apoptosis, the cytoskeleton actively participates in the morphological changes of dying
465 cells. Apoptotic cells also exert a transient pulling force on the apical surface, generating the
466 apicobasal force and increasing tissue tension (Monier et al., 2015). Therefore, we analyzed
467 filamentous actin (F-actin) and myosin using phalloidin and sqh-GFP, a functional tagged
468 version of the myosin regulatory light chain (Royou et al., 2004), respectively, in WT and *hkb*
469 mutant SGs. Compared to WT, we often observed an aberrant accumulation of F-actin and
470 myosin signals along multiple junctions within the SG placode in *hkb* mutants (Figure 3K-O). In
471 addition, there was placode-wide disruption of myosin, including the misshapen supracellular
472 myosin cable that maintains SG tissue integrity (Figure 3L). Apical junctions with increased
473 myosin or F-actin levels often coincided with DCP-1-positive cells (Figure 3M, N-O). Increased
474 F-actin expression was also seen at the apical-lateral membrane of DCP-1 positive cells (Fig.
475 3O), suggesting a potential pulling force along the apicobasal axis by apoptotic cells.

476

477 **Hkb is required for the proper cell cycle status of the SG cells**

478 To further test the impact of *hkb* loss in cytoskeletal organization, we analyzed microtubules,
479 which play a crucial role in forming and maintaining the actomyosin network during tissue
480 invagination (Booth et al., 2014; Ko et al., 2019; Le and Chung, 2021). Interestingly,
481 immunostaining with an antibody against tyrosinated α-tubulin (Tyr-tub), which labels dynamic,
482 short-lived microtubules (Westermann and Weber, 2003) revealed that, in contrast to the strong
483 Tyr-tub signals observed at the apices of WT SG cells (Figure 4A, A'; (Booth et al., 2014; Le
484 and Chung, 2021)), some SG cells in *hkb* mutants lacked apical Tyr-tub signals (Fig. 4B, B').

485 These cells had large, rounded morphology and mislocalized nuclei near the apical surface
486 (Figure 4C, D), indicating cell division. Staining with an antibody against phosphorylated
487 histone H3 (PH3), a marker of mitotic chromatin modification (Gurley et al., 1978), revealed
488 strong PH3 signals in *hkb* mutant SG cells (Figure 4E-H, M), indicating that these cells are
489 actively dividing. Co-staining with Tyr-tub and PH3 revealed that mitotic spindles were
490 consistently aligned parallel to the epithelial sheet (Figure 4K, K'; N=35 cells in metaphase and
491 anaphase in 16 SGs).

492 Mitotic cell rounding and cytokinesis employ processes that reorganize the cytoskeleton,
493 generating forces that locally affect cell rearrangement and tissue morphogenesis (Champion et
494 al., 2017; Pinheiro and Bellaïche, 2018). We observed an increase in F-actin along the apical
495 junctions in PH3-positive SG cells (Figure 4L). Increased F-actin signals were also often
496 detected along the apical-lateral membrane in PH3-positive cells and along the entire membrane
497 of cells in prophase (Figure 4L; red arrowheads in inset). While no biased distribution of
498 dividing cells was observed across the SG placode in *hkb* mutants, dividing cells were more
499 frequently localized in the mid domain compared to the inner or outer domain of the SG (Figure
500 4N, O). SG-specific expression of Hkb in *hkb* mutants reduced the number of PH3-positive cells
501 significantly (Figure 4I, M), suggesting a role for Hkb in inhibiting the mitotic entry of SG cells.

502 Given that apoptosis can induce compensatory cell proliferation in neighboring cells to maintain
503 tissue homeostasis (Haynie and Bryant, 1977; Kondo et al., 2006; Crucianelli et al., 2022), we
504 investigated whether the abnormal cell division in *hkb* mutants was a result of apoptosis. The
505 number of PH3-positive cells in p35-overexpressing SGs in *hkb* mutants was comparable to that
506 in *hkb* mutants alone (Figure 4J, M), suggesting that the abnormal cell division in *hkb* mutants
507 may not be compensatory cell proliferation induced by apoptosis. However, we cannot rule out
508 the possibility that compensatory cell proliferation by a few remaining dying cells still
509 contributes to some of the abnormally dividing cells in *hkb* mutants.

510

511 **Hkb regulates endoreplication progression during SG morphogenesis**

512 The observation of cell division in SG cells was unexpected because SG cells do not divide but
513 rather undergo endoreplication. To further test the cell cycle status in SG cells, we used the Fly-
514 FUCCI system, which allows the identification of different cell cycle phases based on the
515 fluorescent signals of cytoplasmic cyclin B (CycB) and nuclear E2F transcription factor 1 (E2f1)
516 tagged degrons ((Zielke et al., 2014); Figure 5A), as well as 5-Ethynyl-2'-deoxyuridine (EdU)
517 labeling to specifically mark S phase or endocycling cells. Prior to invagination at early stage 11,
518 all WT SG cells exhibited strong nuclear signals for E2f1 and cytoplasmic signals for CycB
519 (Figure 5B-B'') and no EdU signals (Figure 5D), indicating G2 phase. During late stage 11 and
520 stage 12, distal SG cells that had completed invagination showed reduced E2f1 signals and very
521 low levels of CycB (Figure 5F-F''), with high EdU signals (Figure 5H and Figure 5-figure
522 supplement 1A), consistent with a previous finding using BrdU staining (Chandrasekaran and
523 Beckendorf, 2005). By stage 13, nuclear E2f1 signals were almost completely lost in all SG
524 cells, accompanied by low levels of CycB (Figure 5J-J'') and high EdU signals (Figure 5L).
525 These data indicate a distal-to-proximal transition to S phase. At late stage 13, distal SG cells
526 began to show weak E2f1 (arrowheads in Figure 5J') and EdU signals (arrowheads in Figure
527 5L), and by stage 14, most SG cells had regained E2f1 signals (Figure 5N-N'') and lost EdU
528 signals (Figure 5P) except for a few proximal cells (arrowheads in Figure 5 N', P), indicating a
529 distal-to-proximal transition to G2 phase. During stages 15 and 16, almost all SG cells had
530 accumulated E2f1 signals along with increased CycB expression (Figure 5R-R'') and lost EdU
531 signals (Figure 5T). Interestingly, in some late stage SGs, a few distal cells lacked E2f1 signals
532 and showed variable intensity of EdU signals (arrowheads in Figure 5R-R'', T; arrowheads in
533 Figure 5-figure supplement 1E), indicating re-entry into S phase and the onset of a potential
534 second wave of endoreplication. Taken together, our data suggest a distal-to-proximal wave of
535 endoreplication progression during normal SG morphogenesis.

536 In *hkb* mutant SGs, the distal-to-proximal progression of endoreplication was disrupted. It is of
537 note that EdU signals in *hkb* mutants were generally low in the entire embryo and absent in many
538 tissues compared to WT, suggesting endoreplication defects in multiple tissues upon *hkb* loss
539 (Figure 5-figure supplement 1A-I). Similar to WT, most cells in early stage 11 *hkb* mutant SGs
540 exhibited strong nuclear signals for E2f1 and cytoplasmic CycB signals, with little to no EdU
541 signal (Figure 5C-C'', E), except in dividing cells where CycB signals were distributed

542 throughout the entire cell (arrowheads in Figure 5C''), which is consistent with the distribution
543 of CycB during mitosis (Jackman et al., 1995). However, starting at late stage 11 and throughout
544 all stages, almost all SG cells in *hkb* mutants showed nuclear E2f1 signals of varying intensity
545 (Figure 5G-G'', K-K'', O-O''). Consistent with this, a few randomly distributed SG cells in *hkb*
546 mutants showed variable EdU signals, with no clear pattern as seen in WT SGs (Figure 5E, I, M,
547 Q), suggesting that cells either do not enter S phase or enter a weak S phase. Taken together,
548 Hkb plays a critical role in distal-to-proximal endoreplication progression during SG
549 morphogenesis.

550

551 **Regulation of key cell cycle genes by Hkb is critical for cell survival and SG morphogenesis**

552 To understand the mechanisms of endoreplication regulation during SG morphogenesis, we
553 focused on the direct transcriptional targets of Hkb identified by the modENCODE Project using
554 chromatin immunoprecipitation followed by sequencing (ChIP–seq) on the whole embryo
555 (Consortium et al., 2010). Gene Ontology enrichment analysis revealed several key biological
556 processes associated with the defects observed in *hkb* mutants (Figure 6A). Notably, gene
557 clusters related to the cell cycle were identified, including central players like *Cyclin A* (*CycA*),
558 *Cyclin D* (*CycD*), *Cyclin E* (*CycE*), *E2f1*, *aurora A* (*aurA*), and *aurora B* (*aurB*). Additionally,
559 several apoptosis-related genes were identified, including *hid*, *rpr*, and *Death related ICE-like*
560 *caspase* (*Drice*). The full list of Hkb target genes, GO clusters, and the list of genes in each
561 cluster were included in Table S3. Fluorescence in situ hybridization revealed a significant
562 increase in the mRNA levels of *rpr*, *E2f1*, and *CycE* in *hkb* mutant SGs compared to WT at
563 stages 11 and 12 (Figure 6B-J, and Figure 6-figure supplement 1A-H'), suggesting
564 transcriptional repression of these genes by Hkb. *CycA* mRNA levels were increased in some
565 stage 11 SG cells in *hkb* mutants, whereas all WT SG cells of the same stage showed a
566 background level of *CycA* mRNA signals (Figure 6-figure supplement 1I-J').

567 Although not a target of Hkb based on the Chip-seq data, we also tested to see if *hkb* acts as an
568 indirect transcriptional inhibitor of *string* (*stg*), which encodes Cdc25 family protein phosphatase
569 that dephosphorylates and activates Cdk1, triggering entry into mitosis in a post-blastoderm
570 *Drosophila* embryo (Edgar and O'Farrell, 1989; Gautier et al., 1991; Edgar et al. 1994).

571 Consistent with a previous study (Edgar et al. 1994), *stg* mRNA levels were downregulated in
572 the WT SG once invagination began, and this remained true for the *hkb* mutant SG (Figure 6-
573 figure supplement 1K-M), suggesting that the abnormal cell cycle regulation in *hkb* mutants is
574 not due to upregulation of *stg* mRNA levels.

575 Disruption in cell cycle regulation can lead to apoptosis due to errors in DNA replication or
576 failure of DNA integrity checkpoints (Pucci et al., 2000). Immunostaining with a marker of DNA
577 double-strand breaks (γ-H2Av; (Lake et al., 2013)) showed increased levels in *hkb* mutant SGs
578 compared to WT, indicating increased DNA damage (Figure 6-figure supplement 2A-B'). To test
579 whether apoptosis in *hkb* mutant SG cells was triggered by the dysregulation of cell cycle genes,
580 we analyzed double mutants for *hkb* and each of the key Hkb target cyclins and their interacting
581 Cdk genes (*Cdk1* and *Cdk2*). Embryos single mutant for *CycA*, *CycD*, *CycE*, and *Cdk1* showed
582 relatively normal morphology except for a few PH3-positive SG cells in *CycD* and *CycE*
583 mutants, likely due to disrupted cell cycle and abnormal entry into mitosis (Figure 6-figure
584 supplement 3A-F). Embryos double mutant for *hkb* and *CycE* or *Cdk1* rescued the *hkb* mutant
585 phenotypes, but double mutants for *hkb* and *CycA* did not show significant rescue (Figure 6-
586 figure supplement 3I-M, P, Q). *Cdk2* mutant embryos showed severe morphological defects with
587 significantly fewer cells overall, making it difficult to assess differences in the *hkb* mutant
588 background (Figure 6-figure supplement 3G, H). We confirmed the rescue effect by SG-specific
589 knockdown experiments targeting *CycE* and *Cdk1* in *hkb* mutant SGs. As in the double mutant
590 analysis, knockdown of *CycE* resulted in a reduction of both dividing and dying cells (Figure 6K,
591 N, Q, OR, restored the invagination position and led to a partial rescue of the short SG
592 phenotypes (Figure 6K, N; Figure 6-figure supplement 4L-N, X). Similar rescue effects were
593 observed with *Cdk1* knockdown (Figure 6L, O, Q, R and Figure 6-figure supplement 4O-R, X).

594 To further test Hkb's role in cell cycle regulation, we tested Fizzy-related (Fzr), a cell cycle
595 switch that functions with the anaphase-promoting complex (APC) to degrade mitotic cyclins
596 during M and G1 phases and trigger exit from the M phase (Sigrist and Lehner, 1997). Fzr also
597 regulates the transition from the normal cell cycle to the endocycle by degrading mitotic cyclins
598 during G2 phase (Sigrist and Lehner, 1997; Zielke et al., 2011). *fzr* was not a ChiP-Seq target of
599 Hkb, and the *fzr* mRNA levels in the SG were fairly high in both WT and *hkb* mutant embryos.
600 We hypothesized that further overexpression of Fzr in *hkb* mutant SGs could suppress cell

601 division and cell death and rescue the defective tube length phenotype. In support of our
602 hypothesis, overexpression of Fzr in *hkb* mutant SGs resulted in a reduction of both dividing and
603 dying cells, partially rescuing the overall *hkb* mutant phenotypes (Figure 6M, P, Q, R and Figure
604 6-figure supplement 4). When both Fzr and p35 were overexpressed in the *hkb* mutant
605 background to inhibit both mitotic cyclins and cell death, we observed an enhanced rescue effect
606 (Figure 6-figure supplement 4). Overall, these data suggest that the loss of *hkb* leads to the
607 derepression of cyclin/Cdk activities, which disrupts endoreplication and causes SG cells to enter
608 mitosis abnormally (Figure 7). Consequently, cell death occurs in SG cells, leading to disrupted
609 SG morphology.

610 **Discussion**

611 In this study, we have uncovered a previously uncharacterized role for Hkb in coordinating cell
612 cycle regulation and morphogenesis during development. Through a comprehensive analysis of
613 mutant phenotypes, modENCODE ChIP-Seq targets of Hkb, and genetic interaction analyses, we
614 have revealed the role of Hkb in regulating endoreplication to enable proper development of the
615 SG.

616

617 **Hkb regulates the cell cycle through transcriptional and possibly post-translational**
618 **mechanisms**

619 During *Drosophila* embryonic development, many tissues arrest the cell cycle in the G2 phase
620 after the initial cell divisions (Hartenstein and Campos-Ortega, 1985; Edgar and O'Farrell, 1989).
621 Subsequently, several tissues, including the SG, switch to the endocycle. This switch is
622 correlated with the development of three-dimensional organs, suggesting a metabolic need to
623 inhibit active cell proliferation to allow for such a transition during development. Using the Fly-
624 FUCCI system and EdU labeling, we observed progressive endoreplication from distal to
625 proximal regions during normal SG morphogenesis (Figure 5). Our data are consistent with a
626 previous study showing that distal cells enter S phase first during SG invagination
627 (Chandrasekaran and Beckendorf, 2005). Notably, our observation that some distal SG cells in
628 WT re-enter S phase during late SG morphogenesis suggests a potential second wave of
629 endoreplication toward the end of embryogenesis that has not been described. In *hkb* mutant
630 SGs, progressive endoreplication is lost.

631 We propose that endoreplication in SG cells is regulated, at least in part, by Hkb-mediated
632 transcriptional repression of *E2f1* and *CycE* (Figure 6 and Figure 6-figure supplement 1). E2f1 is
633 usually destroyed as cells transit into S phase through degradation by the S-phase activated E3
634 ubiquitin ligase Cullin 4. Whenever E2f1 expression persists in S phase, as is seen with ectopic
635 expression or overexpression of E2f1, cell cycle arrest is disrupted and the rate of cell cycle
636 progression is increased, leading to a significantly higher number of cells in the mitotic phase
637 (Neufeld et al., 1998; Shibutani et al., 2008), as we observed in the *hkb* mutant SG. The changes

638 in the cell cycle control mechanism caused by persistent E2f1 expression during the S phase
639 ultimately lead to widespread apoptosis in affected tissues (Shibutani et al., 2008). During
640 normal SG development, E2f1 and CycE (which is also a transcriptional target of E2f1; Ohtani et
641 al., 1995; Duronio and O'farrell, 1995; Royzman et al., 1997; Duronio et al., 1998) may together
642 control the transition to S phase to begin endoreplication. We propose that Hkb promotes SG cell
643 progression through the S phase, at least in part, through its repression of *E2f1* and *CycE*
644 expression. In support of this, knockdown of *CycE* partially rescued the *hkb* mutant phenotypes
645 (Figure 6).

646 Notably, *stg* transcript levels remain low in *hkb* mutant SGs, suggesting that the abnormal
647 mitotic entry of *hkb* mutant SG cells is not due to *stg* upregulation. We propose that Hkb
648 prevents entry into mitosis, at least in part, by downregulating *CycA* expression. CycA acts in the
649 *Drosophila* G2/M phases of the cell cycle, where it regulates aspects of the DNA replication
650 mechanism and entry into mitosis by binding to Cdk1(Pagano et al., 1992; Knoblich et al., 1994;
651 Yam et al., 2002; Gong and Ferrell Jr, 2010; Bendris et al., 2011; Salle et al., 2012). Loss of *hkb*
652 may prevent inhibition of CycA-Cdk1 activity in the SG. In support of this idea, knockdown of
653 *Cdk1*, or overexpression of *Fzr,* an inhibitor of mitotic cyclins, partially rescued the *hkb* mutant
654 phenotypes (Figure 6). Depletion of the zygotic *CycA* pool did not rescue the *hkb* mutant
655 phenotypes, either because of the contribution of the maternal *CycA* pool or because of the
656 presence of CycB and CycB3, two other cyclins that bind to Cdk1 to regulate mitotic entry.

657 Hkb may regulate the cell cycle not only through transcriptional control of cell cycle genes but
658 also by influencing ubiquitination, a key mechanism of cell cycle regulation. ChIP-Seq analysis
659 revealed that Hkb targets several key components involved in ubiquitination, including *cullin 1*
660 and *archipelago* (*ago*) (Figure 6A; Table S3). Ago is known to regulate CycE levels in
661 *Drosophila* (Moberg et al., 2001). Remarkably, ZnF transcription factors can interact with both
662 nucleic acids and proteins and are important regulators of protein degradation through
663 ubiquitination (Gibson et al., 1988; Iuchi, 2005). Further studies will provide a deeper
664 understanding of the comprehensive mechanisms by which Hkb regulates the cell cycle.

665

666 **Progressive endoreplication during organ formation**

667 Endoreplication in the *Drosophila* embryonic SG, coupled with invagination, allows cells to
668 increase the number of gene copies to provide sufficient proteins for morphogenesis. The
669 regulatory mechanism behind the progressive distal-to-proximal endoreplication in the SG
670 remains unclear. In agreement with Sanchez-Corrales et al., 2021, we observed higher levels of
671 Hkb in the posterior region of the placode at stage 10, which became more uniformly distributed
672 throughout all SG cells by stage 11 (Figure 1-figure supplement 5). The initial difference in Hkb
673 levels within the SG placode may lead to the differential repression of cell cycle genes,
674 contributing to the progression of endoreplication. Alternatively, SG invagination in the
675 dorsal/posterior region could potentially trigger the sequential onset of endoreplication, as
676 suggested by a previous study (Chandrasekaran and Beckendorf, 2005). We observed a
677 disruption in the progressive entry of the SG cells into endoreplication when Hkb function is lost.
678 The degree of disruption varied between samples, with some embryos showing no SG cells in S
679 phase, while others had a small number of SG cells at random positions along the proximal-distal
680 axis with weaker EdU signals compared to WT SGs of similar stages, suggesting that they may
681 be entering a weak S phase (Figure 5). Further investigation of the relationship between
682 endoreplication regulation and SG invagination will provide a better understanding of how cell
683 cycle and morphogenesis coordinate during organ formation. It will also be interesting to test a
684 role for Hkb in cell cycle (endocycle) regulation in other *Drosophila* tissues, and to test a
685 similarly conserved role for the mammalian SP/KLF transcription factors.

686

687 **Hkb's roles in cytoskeletal reorganization and intracellular trafficking**

688 In line with previous studies on the cellular forces exerted by dividing (Kondo and Hayashi,
689 2013; Pinheiro and Bellaïche, 2018) and apoptotic (Monier et al., 2015; Toyama et al., 2008)
690 cells on neighboring cells, the abnormal cell division and excessive cell death observed in *hkb*
691 mutant SGs are associated with a tissue-wide disruption of actomyosin and cell geometry (Figure
692 3). Our data show that the centralized invagination phenotype results primarily from excessive
693 cell death (Figure 2 and Figure 3). However, dividing cells, particularly those near the SG
694 boundary, may contribute to this phenotype by undergoing cell surface area expansion during

695 cell division, increasing the number of cells with larger apical areas along the SG boundary
696 (Figure 4).

697 Based on Hkb ChIP-Seq targets, we propose that Hkb also plays an active role in regulating
698 cytoskeletal organization through transcriptional regulation of key cytoskeletal regulators. Hkb
699 targets include key Rho signaling components and their regulators, such as the small GTPases
700 Rho1 and Rac1, and several RhoGEFs, including RhoGEF2, a key activator of Rho signaling
701 during epithelial morphogenesis (Barrett et al., 1997) (Figure 6A; Table S3). We also propose a
702 critical role for Hkb in regulating intracellular trafficking. Supporting previous research on
703 Hkb's role in regulating Klar, an important regulator of intracellular trafficking (Myat and
704 Andrew, 2002), our data show that Rab11 is mislocalized basally in *hkb* mutant SGs (Figure 2-
705 figure supplement 2). Multiple endocytic components, including *βCOP*, *AP-1-2β*, *AP-2α*, and
706 *Nuf*, as well as several Rab GTPases, including *Rab4*, *Rab10*, *Rab27*, and *Rab30*, were also
707 identified as Hkb ChIP-Seq targets (Figure 6A; Table S3), providing further evidence for the
708 involvement of Hkb in intracellular trafficking. The initial difference in Hkb levels in the SG
709 placode may lead to differential expression of these genes, which could contribute to normal
710 invagination positioning.

711 In conclusion, we have uncovered a role for the Hkb transcription factor in regulating
712 endoreplication and preventing abnormal cell cycle progression during epithelial tube formation.
713 Our findings provide valuable insights into a critical mechanism for coordinating cell cycle
714 regulation and morphogenesis during organ formation.

Acknowledgments

We thank the members of the Chung laboratory for their comments and suggestions. We thank the Bloomington *Drosophila* Stock Center for fly stocks, and D. J. Andrew and the Developmental Studies Hybridoma Bank for antibodies. We thank Flybase and the modENCODE transcription consortium for the gene information and the Hkb ChIP-Seq data. We are grateful to J. C. Larkin and J. L. Woodward for their helpful comments on the manuscript. Cartoons in Figures 1, 5 and 7 were created using Biorender.com. This work was supported by a start-up fund from Louisiana State University and grants from the Louisiana Board of Regents Research Competitiveness Subprogram (LEQSF(2019-22)-RD-A-04) and the National Science Foundation (MCB 2141387) to S.C.

726 **Figure legends**

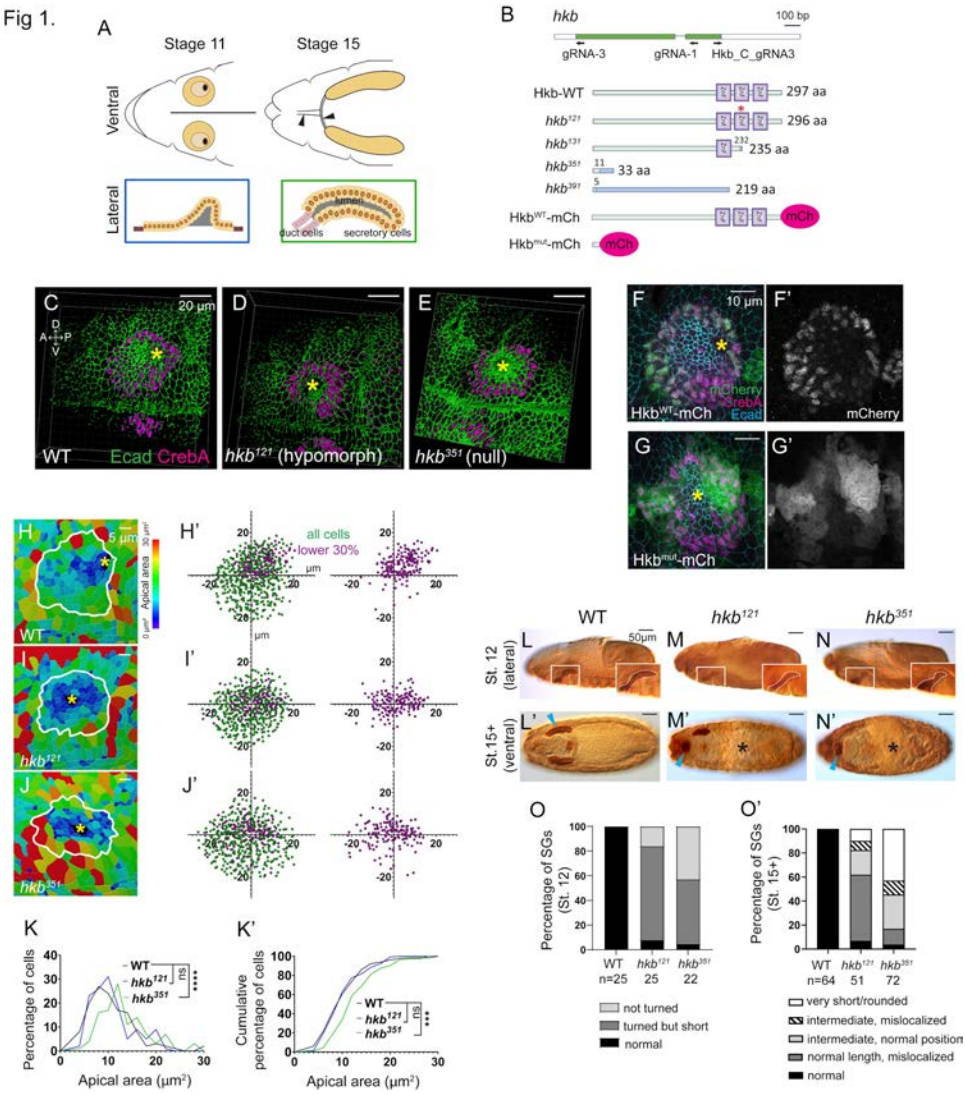

727

728 **Figure 1. Generation of new *hkb* alleles and fluorescent knock-in lines reveals its function**
729 **and tissue-specific localization during SG morphogenesis.** (A) Top cartoon diagram: Anterior
730 region of stage 11 and 15 *Drosophila* embryos. SGs shown in yellow. Brown area, clustered
731 apical constriction of SG cells during invagination. Black, invagination pit. Arrowheads, salivary
732 duct. Bottom cartoon diagram: Lateral view of SG at stages 11 and 15. Orange circles, SG cell
733 nuclei. Gray, SG lumen. (B) Top cartoon diagram: *hkb* transcript displayed with coding exon in
734 green and gRNAs used for *hkb* alleles and mCh knock-in lines. Bottom: Hkb protein structures
735 produced in each allele and knock-in lines. In hkb^{121}, two amino acids (N237 and E238) are
736 substituted with K237 (asterisk). In hkb^{351} and hkb^{391}, a short N-terminal region of the Hkb

737 protein (green) is followed by random amino acid sequences (blue) due to a frameshift. *hkb*
738 mRNA with the premature stop codon in *hkb*^{351} might be degraded by nonsense-mediated
739 mRNA decay. ZnF, zinc finger domain. (C-E) 3D reconstruction of the confocal images of
740 invaginating SGs immunolabeled with Ecad and CrebA. Asterisks, invagination pit. (F-G')
741 Confocal images of stage 11 SGs immunostained for mCh (green), CrebA (magenta), and Ecad
742 (cyan). (H-J) Heat maps showing apical area distribution in invaginating SGs. White lines, SG
743 boundary determined by SG-specific CrebA signals. Yellow asterisks, invagination pits. (H'-J')
744 Scatter plots showing the relative position of cells in the SG placode. X and Y axes represent the
745 distance along the A/P and D/V axes, respectively, from the center of the placode. Cells in the
746 bottom 30% of the apical area (magenta) and all cells (green) are plotted (N = 5 SGs from
747 different embryos (WT, 572 cells; *hkb*^{121}, 505 cells; *hkb*^{351}, 498 cells)). (K, K') Quantification of
748 the apical area distribution in the SG cells of H-J. Mann-Whitney U test (percentage of cells) and
749 Kolmogorov-Smirnov test (cumulative percentage of cells). **, $p<0.01$; ***, $p<0.001$; ****,
750 $p<0.0001$. (L-N') Embryos immunostained for CrebA, with magnified views (insets) showing
751 SGs outlined by white dashed lines. Cyan arrowheads, late-stage SGs. Asterisks, defective gut
752 morphology. (O, O') Quantification of the phenotypic distribution of SGs. n, number of
753 embryos. Statistical significance determined using two-way ANOVA ($p<0.05$).

Fig 2.

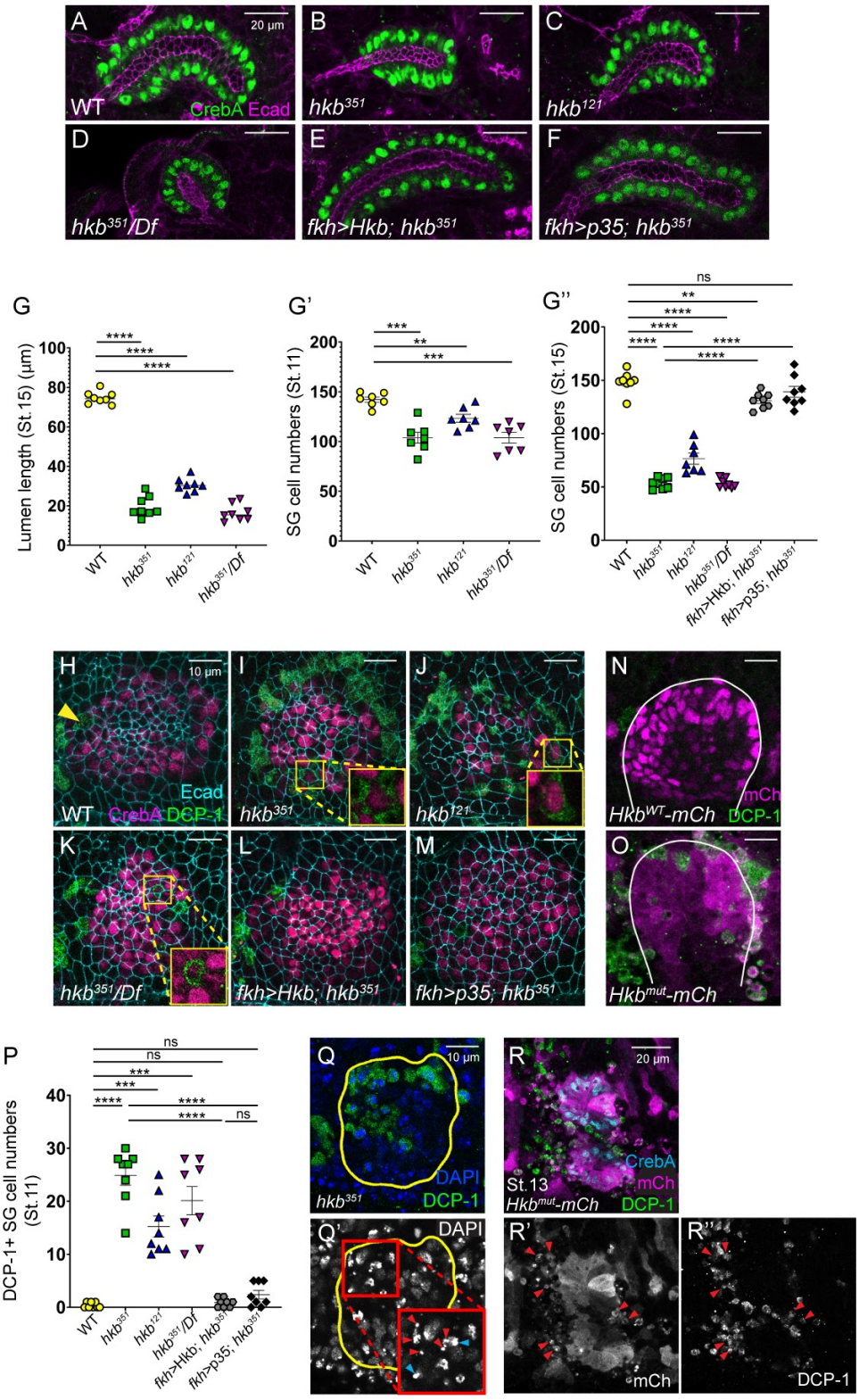
A
20 µm
WT
CrebA Ecad
B
hkb351
C
hkb121
D
hkb351/Df
E
fkh>Hkb; hkb351
F
fkh>p35; hkb351
G
Lumen length (St.15) (µm)
WT
hkb351
hkb121
hkb351/Df
G'
SG cell numbers (St.11)
G''
SG cell numbers (St.15)
fkh>Hkb; hkb351
fkh>p35; hkb351
H
10 µm
Ecad
CrebA DCP-1
I
J
N
mCh
Hkb^WT-mCh
DCP-1
K
L
M
O
Hkb^mut-mCh
P
DCP-1+ SG cell numbers (St.11)
Q
DAPI
DCP-1
Q'
R
20 µm
CrebA
mCh
St.13
R'
R''
mCh
DCP-1

754

755 **Figure 2. Hkb is required to prevent apoptosis in SG cells to ensure proper organ size.** (A-
756 F) Stage 15+ SGs immunolabeled for Ecad (magenta) and CrebA (green). (G) Quantification of
757 the stage 15+ SG lumen length. N=9 (WT), 12 (hkb^{351}), 11 (hkb^{121}), and 8 (hkb^{351}/Df). One-way
758 ANOVA. ****, $p<0.0001$. (G'-G'') Quantification of the number of SG secretory cells at stage
759 11 (G'; N=7 for all genotypes) and stage 15 (G''; N=8 for all genotypes except hkb^{121} (N=7)).
760 One-way ANOVA. **, $p<0.01$; ***, $p<0.001$; ****, $p<0.0001$. (H-M) Pre-invaginating SGs
761 immunolabeled for DCP-1 (green), CrebA (magenta), and Ecad (cyan). Insets, magnified views.
762 (N, O) Hkb^{WT}-mCh and Hkb^{mut}-mCh SGs immunostained for mCh (magenta) and DCP-1
763 (green). White lines, SG boundary determined by SG-specific CrebA signals. (P) Quantification
764 of the DCP-1 positive SG cells. N=8 for all genotypes. One-way ANOVA. ***, $p<0.001$; ****,
765 $p<0.0001$. (Q, Q') Stage 11 *hkb* null mutant SG stained for DAPI (blue) and DCP-1 (green).
766 Insets, higher magnification of the red-boxed region. Red arrowheads, fragmented nuclei. Cyan
767 arrowheads, pyknotic nuclei. Yellow lines, SG boundary determined by SG-specific CrebA
768 signals. (R-R'') SG of a stage 13 Hkb^{mut}-mCh embryo immunostained for mCh (cyan), CrebA
769 (magenta), and DCP-1 (green). Arrowheads, mCh- and DCP-1-positive cells near the SG.

Fig 3.

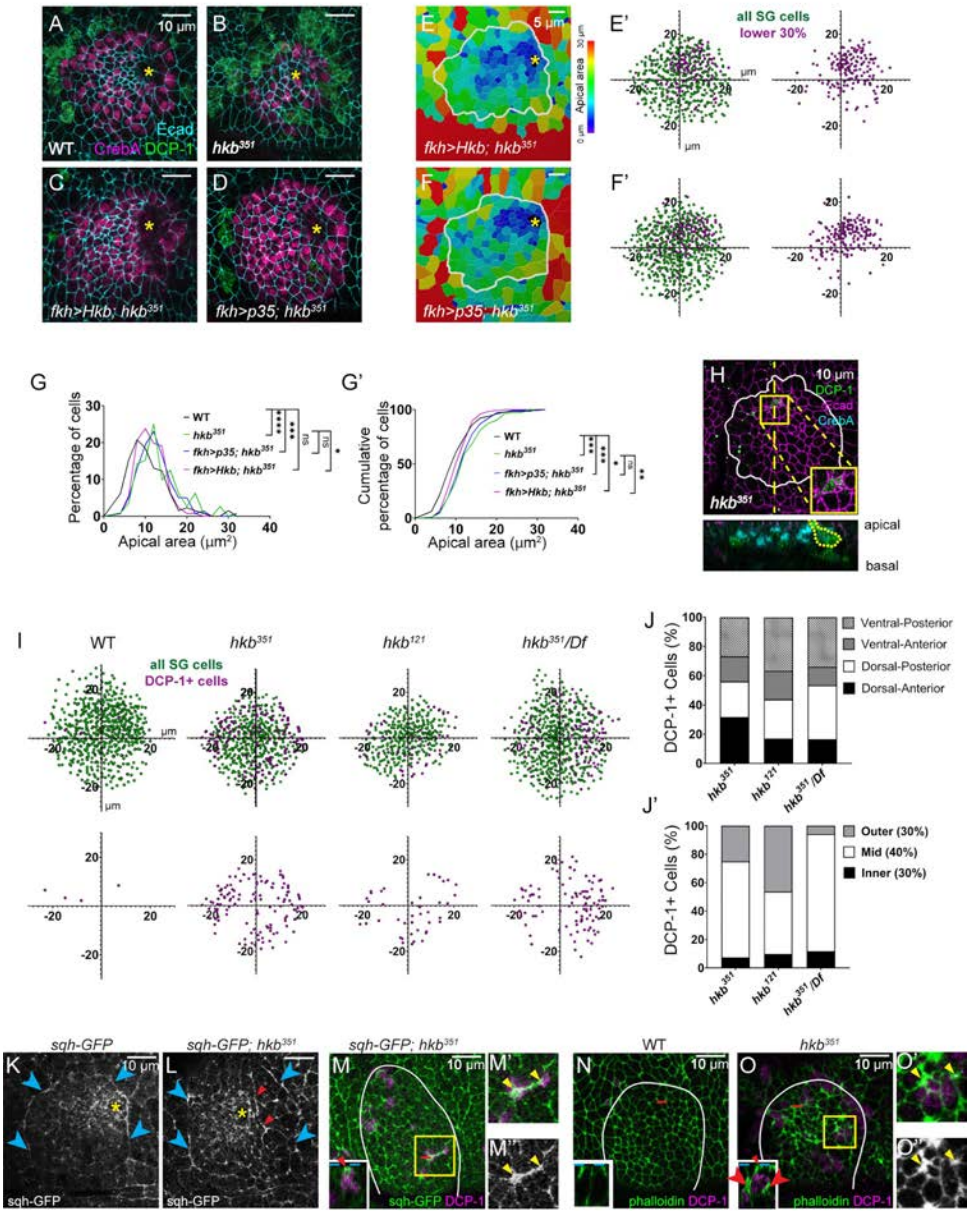

Figure 3. Aberrant cell death results in centered invagination in the *hkb* mutant SG. (A-D) Sstage 11 SGs immunolabeled with DCP-1 (green), CrebA (magenta), and Ecad (cyan). (E-F) Heat maps depicting apical area distribution in invaginating SGs. (E'-F') Scatter plots showing the relative position of cells in the SG placode. X and Y axes represent the distance along the A/P and D/V axes, respectively, from the center of the placode. Cells in the bottom 30% of the apical area (magenta) and all cells (green) are plotted (N=5 SGs from 5 different embryos). (G) *hkb* mutant SG immunostained for DCP-1 (green), Ecad (magenta), and CrebA (cyan). Insets,

778 magnified view of the yellow boxed regions. Z-section along the dotted line displayed below.
779 (H) Scatter plots showing the relative position of total SG cells (green) and DCP-1-positive cells
780 (magenta) in stage 11 SGs. (I, I') Quantification of the number of DCP-1-positive SG cells in
781 different regions of the placode. (J, K) Stage 11 SGs immunostained for GFP (for *sqh-GFP*).
782 Cyan arrowheads, supracellular myosin cable. Red arrowheads, short cables inside the SG
783 placode. Yellow asterisk, invagination pit. (L-L'') Stage 11 SGs immunostained for GFP (for
784 *sqh-GFP*; green) and DCP-1 (magenta). (M-N'') Stage 11 SGs stained for F-actin (green) and
785 DCP-1 (magenta). Insets in L-N, z-sections along red dotted lines. Dotted cyan lines, apical
786 boundary of cells. Red arrowheads/arrows indicate increased myosin (L) and F-actin (N) signals
787 in the apical and lateral regions of the DCP-1-positive cell, respectively. (L', L'', N', N'')
788 Magnified views of yellow boxed regions in L and N. Yellow arrowheads, increased myosin/F-
789 actin signals at the apical-junctional region of DCP-1-positive cells. White lines, SG boundary
790 determined by SG-specific CrebA signals.

Fig 4.

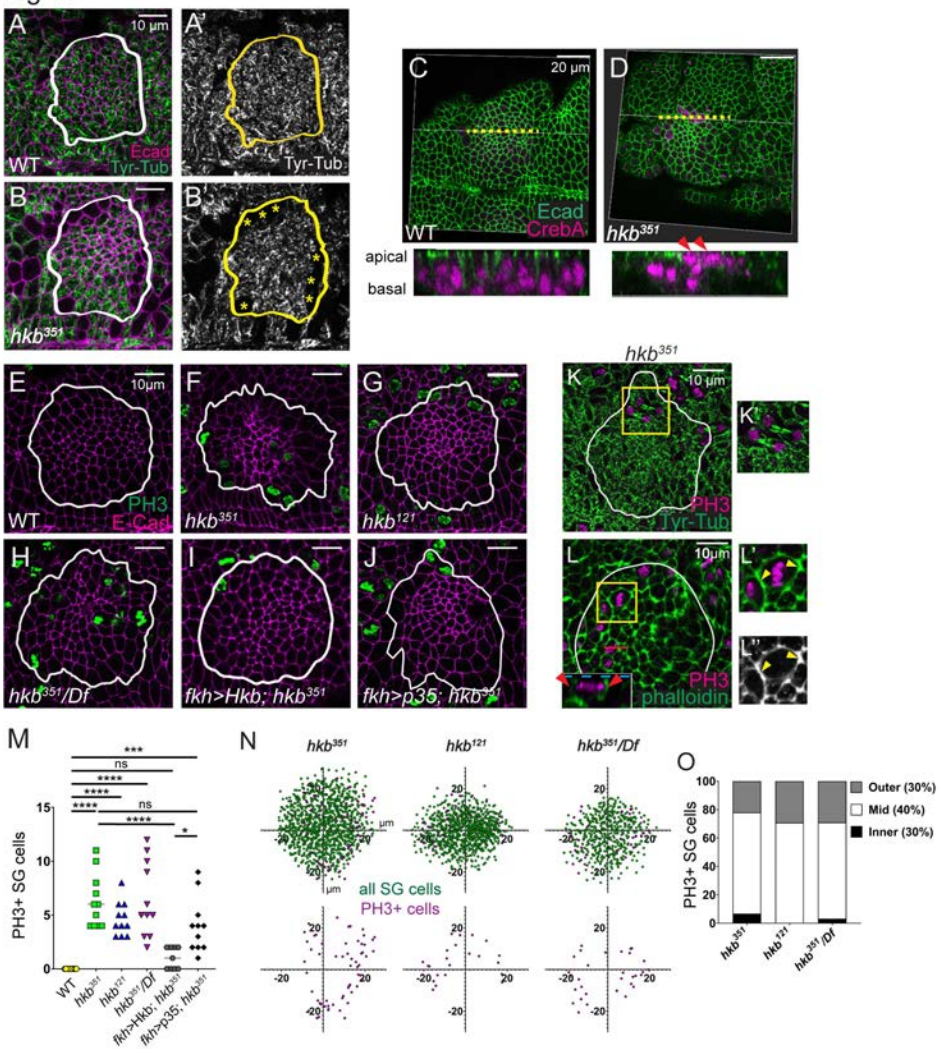

Figure 4. SG cells undergo abnormal cell division in *hkb* mutants. (A-B') Stage 11 SGs immunolabeled with Tyr-Tub (green) and Ecad (magenta). Asterisks, cells without Tyr-Tub signals. (C, D) 3D reconstructions of confocal images of pre-invaginating SGs immunolabeled with Ecad (green) and CrebA (magenta). Z-sections along yellow dotted lines shown below. Arrowheads, apically localizing nuclei in *hkb* mutant SG. (E-J) Stage 11 SGs immunolabeled with PH3 (green) and Ecad (magenta). (K, K') Stage 11 SGs immunolabeled with Tyr-Tub (green) and PH3 (magenta). Higher magnification of yellow boxed region shown in K'. (L-L'') Stage 11 SGs immunolabeled with PH3 (magenta) and phalloidin (green). Inset; lateral section (XZ; red line). Higher magnification of yellow boxed region shown in L' and L''. (M) Quantification of the number of PH3-positive SG cells. N=11 for all genotypes except *fkh*>Hkb; *hkb*^{351}(N=9). One-way ANOVA. **, $p<0.01$; ***, $p<0.001$; ****, $p<0.0001$. (N) Scatter plots

803 showing the position of total SG cells (green) and PH3-positive cells (magenta) in the SG
804 placode. X and Y axes represent the distance along the A/P and D/V axes, respectively, from the
805 center of the placode (N=5 SGs from 5 different embryos). (O) Quantification of the number of
806 PH-positive SG cells in different regions of the placode. White and yellow lines, SG boundary
807 determined by SG-specific CrebA signals.

808

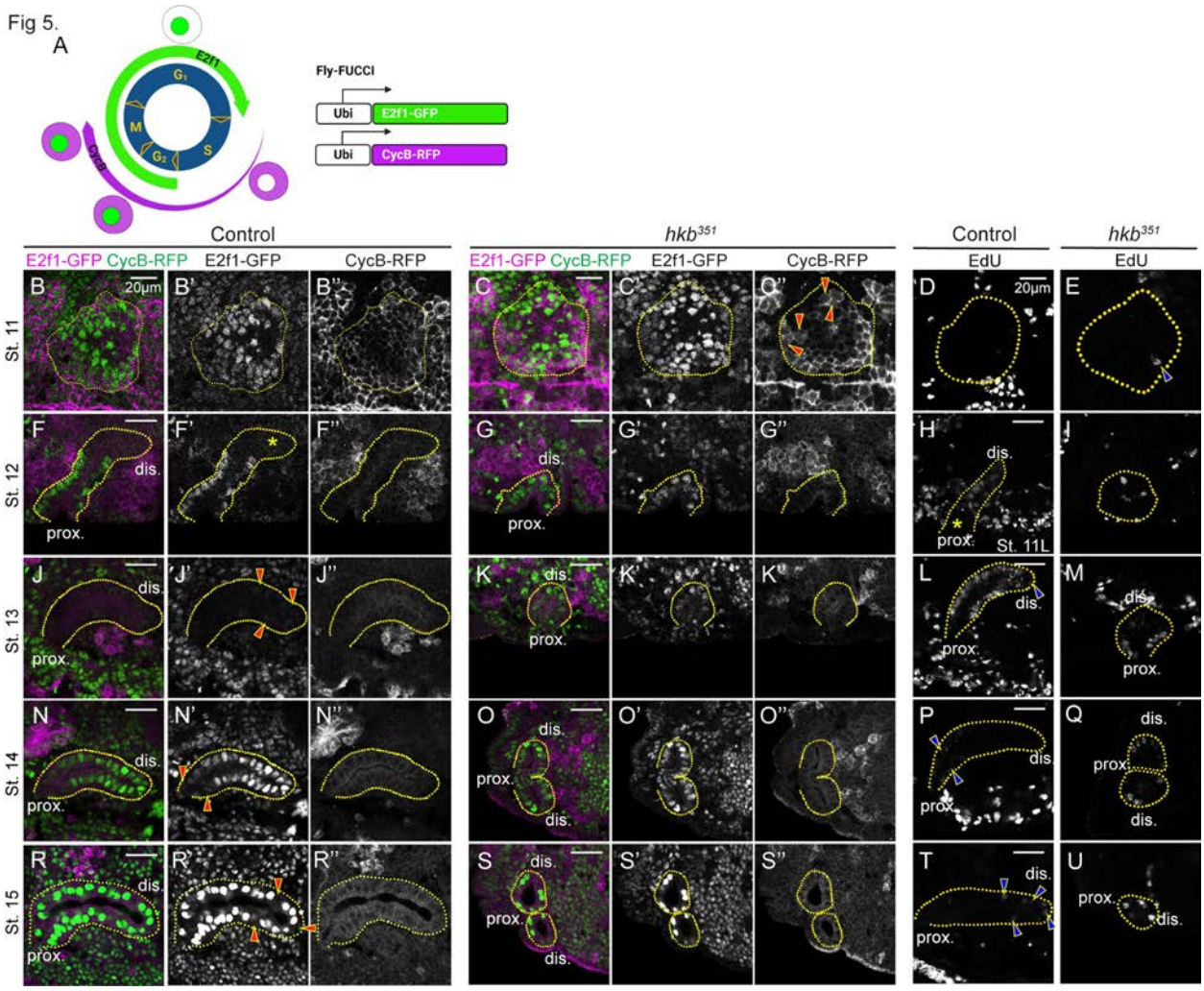

809

810 **Figure 5. The distal-to-proximal progression of the endoreplication is disrupted in the *hkb***
811 **mutant SG.** (A) Schematic of the Fly-FUCCI system. (B-C'', F-G'', J-K'', N-O'', R-S'') SGs
812 immunolabeled with GFP (for E2f1-GFP; green) and CycB (for CycB-RFP; magenta) at
813 different stages. Red arrowheads in C'', CycB signals distributed throughout the dividing cells.
814 Asterisk in F', absence of E2F1 signals in distal cells of stage 12 SG. Red arrowheads in J', weak
815 E2f1 signals in the proximal SG cells. Red arrowheads in N' and R', little to no E2f1 signal in
816 proximal (N') and distal (R') SG cells. (D-E, H-I, L-M, P-Q, T-U) EdU-labeled SGs at different
817 developmental stages. Blue arrowhead in E, EdU-positive single SG cell. Asterisks in H, absence
818 of EdU signals in proximal cells of late stage 11 SG. Blue arrowheads in L, P and T, weak EdU
819 signals in distal (L, T) and proximal (P) SG cells. Yellow dotted lines, SG boundary determined
820 by SG-specific CrebA signals. Due to the proximity of the two SGs in *hkb* mutants, one or two

821 SGs are shown depending on the orientation of the embryo. dis. denotes distal; prox. denotes
822 proximal.

823

824

825

826

827

828

829

830

Fig 6.

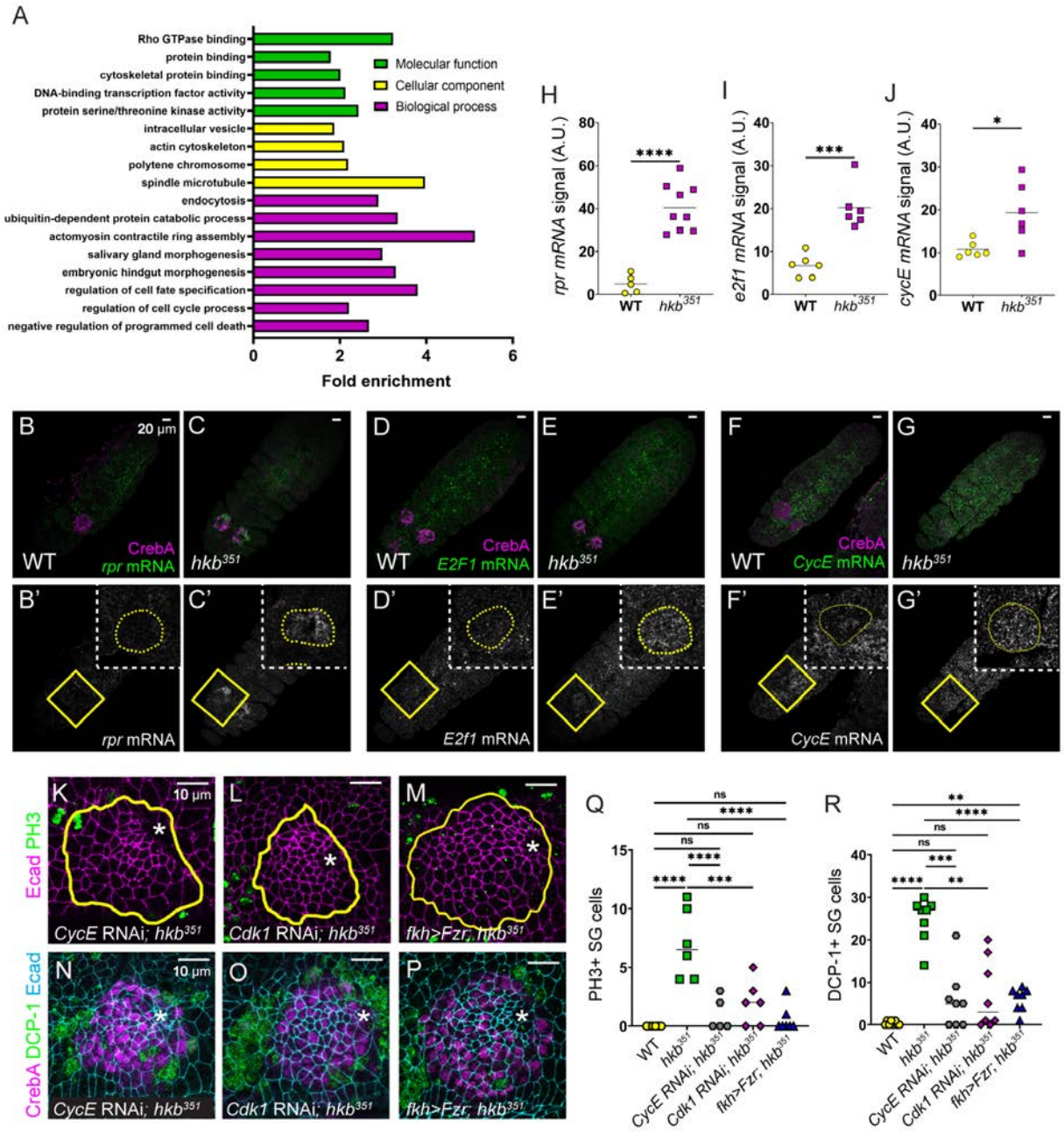

Figure. 6. Hkb regulates key cell cycle and cell death genes transcriptionally. (A) GO enrichment analysis of ModENCODE Hkb ChIP-Seq data. (B-G'') Fluorescence *in situ* hybridization images of stage 11 embryos showing mRNA levels of *rpr* (B-C'), *E2f1* (D-E'), and *CycE* (F-G'). Yellow boxed regions shown at a higher magnification in insets. (H-J) Quantification of the signal intensity of the mRNA levels shown in B'-G'. N=5 (WT) and 9 SGs (*hkb*^{351}) (H); 6 SGs for both genotypes (I, J). Student's t-test with Welch's correction. **, p<0.01;

838 ***, $p<0.001$; ****, $p<0.0001$. (K-P) *Cdk1* and *CycE* knockdowns and Fzr overexpression in
839 *hkb* mutant SGs immunostained for Ecad (magenta) and PH3 (green) (K-M) and Ecad (magenta),
840 DCP-1 (green), and CrebA (cyan) (N-P). Asterisks, invagination pit. (Q, R) Quantification of the
841 number of PH3-positive (Q) and DCP-1-positive (R) SG cells. N=6 (Q) and 8 (R) SGs from
842 different embryos for all genotypes. One-way ANOVA. **, $p<0.01$; ***, $p<0.001$; ****,
843 $p<0.0001$. Yellow lines and yellow dotted lines, SG boundary determined by SG-specific CrebA
844 signals.

Fig 7.

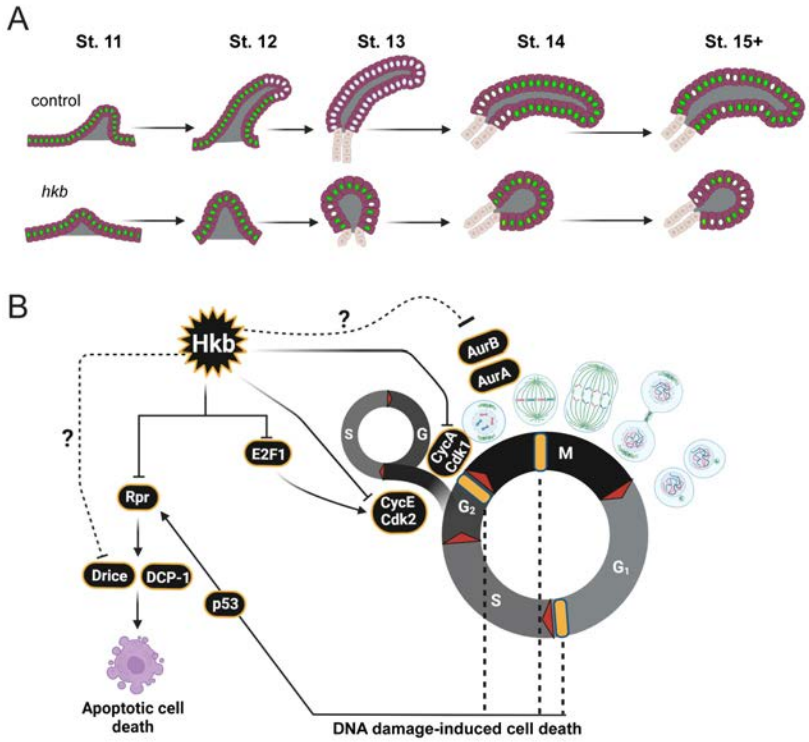

Figure 7. A model of endoreplication regulation by Hkb during SG morphogenesis. (A) Cartoon diagram showing the cell cycle status and progression of endoreplication during SG morphogenesis. Cells with green nuclei represent cells with E2f1 signals (G phase). Cells with white nuclei represent cells with EdU signals (S phase). (B) Summary of the role of Hkb in cell cycle regulation in the SG. Hkb helps to inhibit cell division and cell death and promotes endoreplication progression through transcriptional inhibition of key cell cycle and pro-apoptotic genes. Cell death in *hkb* mutant SG may also be caused by DNA damage-induced cell death. Yellow bars represent cell cycle checkpoints.

855 **Table S1. Fly strains used**

Fly strain	**Sources and References**	**RRID**
Oregon R (wild type)		
fkh-Gal4	Henderson and Andrew, 2000	BDSC_78060
hkb^{121}	This study	
hkb^{131}	This study	
hkb^{351}	This study	
hkb^{391}	This study	
Hkb^{WT}*-mCh*	This study	
Hkb^{mut}*-mCh*	This study	
hkb^{2}	Weigel et al., 1990	
hkb^{A321R1}	Gaul and Weigel, 1991	
UAS-p35		BDSC_5072
UAS-Hkb	Myat and Andrew, 2002	
$CycE^{AR95}$		BDSC_6637
$CycD^{1}$		BDSC_55125
$CycA^{C8LR1}$		BDSC_6627
$Cdk1^{B47}$		BDSC_6643
TRiP.GL00511 (UAS-CycE RNAi)		BDSC_36092
TRiP.HMS01531 (*UAS-Cdk1 RNAi*)		BDSC_36117

UAS-Fzr		BDSC_91688
Ubi-GFP.E2f1, Ubi-mRFP1.CycB		BDSC_55098

856

857 **Table S2. Antibodies Used**

Antibody	Source	RRID	Dilution
α-Ecad (rat)	DSHB (DCAD2)	AB_528120	1:50
α-CrebA (rat)	Andrew lab (John Hopkins University); re-made in this study		1:3,000
α-CrebA (rabbit)	Andrew lab (John Hopkins University)	AB_10805295	1:5,000
α-CrebA (guinea pig)	This study		1:5,000
α-GFP (mouse)	Invitrogen (A11120)	AB_221568	1:500
α-GFP (chicken)	Invitrogen (A10262)	AB_2534023	1:1,000
α-RFP (rabbit)	Invitrogen (R10367)	AB_10563941	1: 2,000
α-β-galactosidase (rabbit)	Invitrogen (A11132)	AB_221539	1:500
α-β-galactosidase (mouse)	Invitrogen (MA5-15222)	AB_10980770	1:500
α-mCherry (rat)	Invitrogen (M11217)	AB_2536611	1:1,000
α-mCherry (rabbit)	Invitrogen (PA534974)	AB_2552323	1:1,000
α-DCP-1 (rabbit)	Cell signaling technology (9578)	AB_2721060	1:200
α-phosphohistone 3 (rabbit)	Invitrogen (PA517869)	AB_10984484	1:1,000
α-tyrosinated α-tubulin (rat)	Invitrogen (MA1-80017)	AB_2210201	1:1,000
α-H2AvD (mouse)	DSHB (UNC93-5.2.1)	AB_2618077	1: 1,000

α-Sage (guinea pig)	Andrew lab (Johns Hopkins University)		1: 100
α-CyclinB (mouse)	DSHB (F2F4)	AB_528189	1: 5
α-Crb (mouse)	DSHB (Cq4)	AB_528181	1:10
α-Rab11 (rabbit)	Andrew lab (John Hopkins University)		1:500
α-mCherry (rat)	Invitrogen (M11217)	AB_2536611	1:1,000
α-mCherry (rabbit)	Invitrogen (PA534974)	AB_2552323	1:1,000
α-α-Spectrin (mouse)	DSHB (3A9)	AB_528473	1:2
α-Dead Ringer (chicken)	Andrew lab (Johns Hopkins University)		1:1000
Phalloidin Alexa 488	Invitrogen (A12379)		1:250
Alexa Fluor 488/568/647-coupled secondary antibodies	Invitrogen		1:500

858

References

ANDREW, D. J. & EWALD, A. J. 2010. Morphogenesis of epithelial tubes: Insights into tube formation, elongation, and elaboration. *Developmental biology,* 341**,** 34-55.

BAENA-LOPEZ, L. A., ALEXANDRE, C., MITCHELL, A., PASAKARNIS, L. & VINCENT, J.-P. 2013. Accelerated homologous recombination and subsequent genome modification in Drosophila. *Development,* 140**,** 4818-4825.

BARRETT, K., LEPTIN, M. & SETTLEMAN, J. 1997. The Rho GTPase and a putative RhoGEF mediate a signaling pathway for the cell shape changes in Drosophila gastrulation. *Cell,* 91**,** 905-915.

BENDRIS, N., LEMMERS, B., BLANCHARD, J.-M. & ARSIC, N. 2011. Cyclin A2 mutagenesis analysis: a new insight into CDK activation and cellular localization requirements. *PloS one,* 6**,** e22879.

BOOTH, A. J., BLANCHARD, G. B., ADAMS, R. J. & RÖPER, K. 2014. A dynamic microtubule cytoskeleton directs medial actomyosin function during tube formation. *Developmental cell,* 29**,** 562-576.

BRÖNNER, G., CHU-LAGRAFF, Q., DOE, C. Q., COHEN, B., WEIGEL, D., TAUBERT, H. & JÄCKLE, H. 1994. Sp1/egr-like zinc-finger protein required for endoderm specification and germ-layer formation in Drosophila. *Nature,* 369**,** 664-668.

CHAMPION, L., LINDER, M. I. & KUTAY, U. 2017. Cellular reorganization during mitotic entry. *Trends in cell biology,* 27**,** 26-41.

CHANDRASEKARAN, V. & BECKENDORF, S. K. 2003. senseless is necessary for the survival of embryonic salivary glands in Drosophila. *Development,* 130**,** 4719-4728.

CHANDRASEKARAN, V. & BECKENDORF, S. K. 2005. Tec29 controls actin remodeling and endoreplication during invagination of the Drosophila embryonic salivary glands.

CHUNG, S., HANLON, C. D. & ANDREW, D. J. 2014. Building and specializing epithelial tubular organs: the Drosophila salivary gland as a model system for revealing how epithelial organs are specified, form and specialize. *Wiley Interdisciplinary Reviews: Developmental Biology,* 3**,** 281-300.

CHUNG, S., KIM, S. & ANDREW, D. J. 2017. Uncoupling apical constriction from tissue invagination. *Elife,* 6**,** e22235.

CONSORTIUM, M., ROY, S., ERNST, J., KHARCHENKO, P. V., KHERADPOUR, P., NEGRE, N., EATON, M. L., LANDOLIN, J. M., BRISTOW, C. A. & MA, L. 2010. Identification of functional elements and regulatory circuits by Drosophila modENCODE. *Science,* 330**,** 1787-1797.

CRUCIANELLI, C., JAISWAL, J., VIJAYAKUMAR MAYA, A., NOGAY, L., COSOLO, A., GRASS, I. & CLASSEN, A.-K. 2022. Distinct signaling signatures drive compensatory proliferation via S-phase acceleration. *PLoS Genetics,* 18**,** e1010516.

DE IACO, R., SOUSTELLE, L., KAMMERER, M., SORRENTINO, S., JACQUES, C. & GIANGRANDE, A. 2006. Huckebein-mediated autoregulation of Glide/Gcm triggers glia specification. The EMBO Journal, 25, 244-254.

DURONIO, R. J., O'FARRELL, P. H., XIE, J.-E., BROOK, A. & DYSON, N. 1995. The transcription factor E2F is required for S phase during Drosophila embryogenesis. *Genes & development,* 9**,** 1445-1455.

DURONIO, R. & O'FARRELL, P. 1995. Developmental control of the G1 to S transition in Drosophila. Genes Dev., 9, 1456-1468.

904 DURONIO, R. J., BONNETTE, P. C. & O'FARRELL, P. H. 1998. Mutations of the Drosophila
905 dDP, dE2F, and cyclin E genes reveal distinct roles for the E2F-DP transcription factor
906 and cyclin E during the G1-S transition. Molecular and Cellular Biology, 18, 141-151.
907 EDGAR, B. A. & O'FARRELL, P. H. 1989. Genetic control of cell division patterns in the
908 Drosophila embryo. *Cell,* 57**,** 177-187.
909 FOLLETTE, P. J., DURONIO, R. J. & O'FARRELL, P. H. 1998. Fluctuations in cyclin E levels
910 are required for multiple rounds of endocycle S phase in Drosophila. *Current Biology,* 8**,**
911 235-238.
912 FOX, R. M., VAISHNAVI, A., MARUYAMA, R. & ANDREW, D. J. 2013. Organ-specific
913 gene expression: the bHLH protein Sage provides tissue specificity to Drosophila FoxA.
914 *Development,* 140**,** 2160-2171.
915 GANDARILLAS, A., MOLINUEVO, R. & SANZ-GÓMEZ, N. 2018. Mammalian
916 endoreplication emerges to reveal a potential developmental timer. *Cell Death &*
917 *Differentiation,* 25**,** 471-476.
918 GAUL, U. & WEIGEL, D. 1990. Regulation of Krüppel expression in the anlage of the
919 Malpighian tubules in the Drosophila embryo. *Mechanisms of development,* 33**,** 57-67.
920 GIBSON, T. J., POSTMA, J. P., BROWN, R. S. & ARGOS, P. 1988. A model for the tertiary
921 structure of the 28 residue DNA-binding motif ('zinc finger') common to many
922 eukaryotic transcriptional regulatory proteins. *Protein Engineering, Design and*
923 *Selection,* 2**,** 209-218.
924 GIRDLER, G. C. & RÖPER, K. Controlling cell shape changes during salivary gland tube
925 formation in Drosophila. Seminars in Cell & Developmental Biology, 2014. Elsevier,
926 74-81.
927 GODARD, B. G. & HEISENBERG, C.-P. 2019. Cell division and tissue mechanics. *Current*
928 *opinion in cell biology,* 60**,** 114-120.
929 GONG, D. & FERRELL JR, J. E. 2010. The roles of cyclin A2, B1, and B2 in early and late
930 mitotic events. *Molecular biology of the cell,* 21**,** 3149-3161.
931 GREGORY, S. L., KORTSCHAK, R. D., KALIONIS, B. & SAINT, R. 1996. Characterization
932 of the dead ringer gene identifies a novel, highly conserved family of sequence-specific
933 DNA-binding proteins. *Molecular and cellular biology,* 16**,** 792-799.
934 GURLEY, L. R., D'ANNA, J. A., BARHAM, S. S., DEAVEN, L. L. & TOBEY, R. A. 1978.
935 Histone phosphorylation and chromatin structure during mitosis in Chinese hamster cells.
936 *European journal of biochemistry,* 84**,** 1-15.
937 HARTENSTEIN, V. & CAMPOS-ORTEGA, J. A. 1985. Fate-mapping in wild-type Drosophila
938 melanogaster: I. The spatio-temporal pattern of embryonic cell divisions. *Wilhelm Roux's*
939 *archives of developmental biology,* 194**,** 181-195.
940 HAYNIE, J. L. & BRYANT, P. J. 1977. The effects of X-rays on the proliferation dynamics of
941 cells in the imaginal wing disc of Drosophila melanogaster. *Wilhelm Roux's archives of*
942 *developmental biology,* 183**,** 85-100.
943 HENDERSON, K. D. & ANDREW, D. J. 2000. Regulation and function of Scr, exd, and hth in
944 the Drosophila salivary gland. *Developmental biology,* 217**,** 362-374.
945 HERRIGES, M. & MORRISEY, E. E. 2014. Lung development: orchestrating the generation
946 and regeneration of a complex organ. *Development,* 141**,** 502-513.
947 HUH, J. R., GUO, M. & HAY, B. A. 2004. Compensatory proliferation induced by cell death in
948 the Drosophila wing disc requires activity of the apical cell death caspase Dronc in a
949 nonapoptotic role. *Current Biology,* 14**,** 1262-1266.

950 ISMAT, A., CHESHIRE, A. M. & ANDREW, D. J. 2013. The secreted AdamTS-A
951 metalloprotease is required for collective cell migration. *Development,* 140**,** 1981-1993.
952 IUCHI, S. 2005. C2H2 zinc fingers as DNA binding domains. *Zinc finger proteins: From atomic*
953 *contact to cellular function.* Springer.
954 JACKMAN, M., FIRTH, M. & PINES, J. 1995. Human cyclins B1 and B2 are localized to
955 strikingly different structures: B1 to microtubules, B2 primarily to the Golgi apparatus.
956 *The EMBO journal,* 14**,** 1646-1654.
957 KO, C. S., TSERUNYAN, V. & MARTIN, A. C. 2019. Microtubules promote intercellular
958 contractile force transmission during tissue folding. *Journal of Cell Biology,* 218**,** 2726-
959 2742.
960 KONDO, S., SENOO-MATSUDA, N., HIROMI, Y. & MIURA, M. 2006. DRONC coordinates
961 cell death and compensatory proliferation. *Molecular and cellular biology,* 26**,** 7258-
962 7268.
963 KONDO, T. & HAYASHI, S. 2013. Mitotic cell rounding accelerates epithelial invagination.
964 *Nature,* 494**,** 125-129.
965 LAKE, C. M., KORDA HOLSCLAW, J., BELLENDIR, S. P., SEKELSKY, J. & HAWLEY, R.
966 S. 2013. The development of a monoclonal antibody recognizing the Drosophila
967 melanogaster phosphorylated histone H2A variant (γ-H2AV). *G3: Genes, Genomes,*
968 *Genetics,* 3**,** 1539-1543.
969 LE, T. P. & CHUNG, S. 2021. Regulation of apical constriction via microtubule-and Rab11-
970 dependent apical transport during tissue invagination. *Molecular Biology of the Cell,* 32**,**
971 1033-1047.
972 LEGOFF, L. & LECUIT, T. 2015. Mechanical forces and growth in animal tissues. Cold Spring
973 Harb. Perspect. Biol. 8, a019232.
974 MAO, Y., TOURNIER, A. L., HOPPE, A., KESTER, L., THOMPSON, B. J. & TAPON, N.
975 2013. Differential proliferation rates generate patterns of mechanical tension that orient
976 tissue growth. *The EMBO journal,* 32**,** 2790-2803.
977 MARINARI, E., MEHONIC, A., CURRAN, S., GALE, J., DUKE, T. & BAUM, B. 2012. Live-
978 cell delamination counterbalances epithelial growth to limit tissue overcrowding. *Nature,*
979 484**,** 542-545.
980 MARUYAMA, R., GREVENGOED, E., STEMPNIEWICZ, P. & ANDREW, D. J. 2011.
981 Genome-wide analysis reveals a major role in cell fate maintenance and an unexpected
982 role in endoreduplication for the Drosophila FoxA gene Fork head. *PloS one,* 6**,** e20901.
983 MASSA, V., SAVERY, D., YBOT-GONZALEZ, P., FERRARO, E., RONGVAUX, A.,
984 CECCONI, F., FLAVELL, R., GREENE, N. D. & COPP, A. J. 2009. Apoptosis is not
985 required for mammalian neural tube closure. *Proceedings of the National Academy of*
986 *Sciences,* 106**,** 8233-8238.
987 MONIER, B., GETTINGS, M., GAY, G., MANGEAT, T., SCHOTT, S., GUARNER, A. &
988 SUZANNE, M. 2015. Apico-basal forces exerted by apoptotic cells drive epithelium
989 folding. *Nature,* 518**,** 245-248.
990 MYAT, M. M. & ANDREW, D. J. 2000a. Fork head prevents apoptosis and promotes cell shape
991 change during formation of the Drosophila salivary glands. *Development,* 127**,** 4217-
992 4226.
993 MYAT, M. M. & ANDREW, D. J. 2000b. Organ shape in the Drosophila salivary gland is
994 controlled by regulated, sequential internalization of the primordia. *Development,* 127**,**
995 679-691.

MYAT, M. M. & ANDREW, D. J. 2002. Epithelial tube morphology is determined by the polarized growth and delivery of apical membrane. *Cell,* 111**,** 879-891.

NEUFELD, T. P., DE LA CRUZ, A. F. A., JOHNSTON, L. A. & EDGAR, B. A. 1998. Coordination of growth and cell division in the Drosophila wing. Cell, 93, 1183-1193.

NIKOLOPOULOU, E., GALEA, G. L., ROLO, A., GREENE, N. D. & COPP, A. J. 2017. Neural tube closure: cellular, molecular and biomechanical mechanisms. *Development,* 144**,** 552-566.

OHTANI, K., DEGREGORI, J. & NEVINS, J. R. 1995. Regulation of the cyclin E gene by transcription factor E2F1. *Proceedings of the National Academy of Sciences,* 92**,** 12146-12150.

PAGANO, M., PEPPERKOK, R., VERDE, F., ANSORGE, W. & DRAETTA, G. 1992. Cyclin A is required at two points in the human cell cycle. *The EMBO journal,* 11**,** 961-971.

PINHEIRO, D. & BELLAÏCHE, Y. 2018. Mechanical force-driven adherens junction remodeling and epithelial dynamics. *Developmental cell,* 47**,** 3-19.

PIRRAGLIA, C., WALTERS, J. & MYAT, M. M. 2010. Pak1 control of E-cadherin endocytosis regulates salivary gland lumen size and shape. *Development,* 137**,** 4177-4189.

PRADHAN, R., KUMAR, S. & MATHEW, R. 2023. Lateral adherens junctions mediate a supracellular actomyosin cortex in drosophila trachea. *iScience,* 26.

PUCCI, B., KASTEN, M. & GIORDANO, A. 2000. Cell cycle and apoptosis. *Neoplasia,* 2**,** 291-299.

RÖPER, K. 2012. Anisotropy of Crumbs and aPKC drives myosin cable assembly during tube formation. *Developmental cell,* 23**,** 939-953.

ROYOU, A., FIELD, C., SISSON, J. C., SULLIVAN, W. & KARESS, R. 2004. Reassessing the role and dynamics of nonmuscle myosin II during furrow formation in early Drosophila embryos. *Molecular biology of the cell,* 15**,** 838-850.

ROYZMAN, I., WHITTAKER, A. J. & ORR-WEAVER, T. L. 1997. Mutations in Drosophila DP and E2F distinguish G1–S progression from an associated transcriptional program. Genes & development, 11, 1999-2011.

RYOO, H. D., GORENC, T. & STELLER, H. 2004. Apoptotic cells can induce compensatory cell proliferation through the JNK and the Wingless signaling pathways. *Developmental cell,* 7**,** 491-501.

SANCHEZ-CORRALES, Y. E., BLANCHARD, G. B. & RÖPER, K. 2018. Radially patterned cell behaviours during tube budding from an epithelium. *Elife,* 7**,** e35717.

SANCHEZ-CORRALES, Y. E., BLANCHARD, G. B. & RÖPER, K. 2021. Correct regionalization of a tissue primordium is essential for coordinated morphogenesis. *Elife,* 10.

SARKISSIAN, T., TIMMONS, A., ARYA, R., ABDELWAHID, E. & WHITE, K. 2014. Detecting apoptosis in Drosophila tissues and cells. *Methods,* 68**,** 89-96.

SHIBUTANI, S. T., DE LA CRUZ, A. F. A., TRAN, V., TURBYFILL, W. J., REIS, T., EDGAR, B. A. & DURONIO, R. J. 2008. Intrinsic negative cell cycle regulation provided by PIP box-and Cul4Cdt2-mediated destruction of E2f1 during S phase. Developmental cell, 15, 890-900.

SIDOR, C. & RÖPER, K. 2016. Genetic control of salivary gland tubulogenesis in Drosophila. *Organogenetic Gene Networks.* Springer.

1040 SIDOR, C., STEVENS, T. J., JIN, L., BOULANGER, J. & RÖPER, K. 2020. Rho-kinase planar
1041 polarization at tissue boundaries depends on phospho-regulation of membrane residence
1042 time. *Developmental cell,* 52**,** 364-378. e7.
1043 SIGRIST, S. J. & LEHNER, C. F. 1997. Drosophila fizzy-related down-regulates mitotic cyclins
1044 and is required for cell proliferation arrest and entry into endocycles. *Cell,* 90**,** 671-681.
1045 SLATTUM, G., MCGEE, K. M. & ROSENBLATT, J. 2009. P115 RhoGEF and microtubules
1046 decide the direction apoptotic cells extrude from an epithelium. *Journal of Cell Biology,*
1047 186**,** 693-702.
1048 SMITH, A. V. & ORR-WEAVER, T. L. 1991. The regulation of the cell cycle during Drosophila
1049 embryogenesis: the transition to polyteny. *Development,* 112**,** 997-1008.
1050 SPINA, E. & COWIN, P. Embryonic mammary gland development. Seminars in Cell &
1051 Developmental Biology, 2021. Elsevier, 83-92.
1052 TOYAMA, Y., PERALTA, X. G., WELLS, A. R., KIEHART, D. P. & EDWARDS, G. S. 2008.
1053 Apoptotic force and tissue dynamics during Drosophila embryogenesis. *Science,* 321**,**
1054 1683-1686.
1055 VISHWAKARMA, V., LE, T. P. & CHUNG, S. 2022. Multifunctional role of GPCR signaling
1056 in epithelial tube formation. *Development,* 149**,** dev200519.
1057 WEIGEL, D., SEIFERT, E., REUTER, D. & JÄCKLE, H. 1990. Regulatory elements
1058 controlling expression of the Drosophila homeotic gene fork head. *The EMBO Journal,* 9**,**
1059 1199-1207.
1060 WESTERMANN, S. & WEBER, K. 2003. Post-translational modifications regulate microtubule
1061 function. *Nature reviews Molecular cell biology,* 4**,** 938-948.
1062 WILDE, J. J., PETERSEN, J. R. & NISWANDER, L. 2014. Genetic, epigenetic, and
1063 environmental contributions to neural tube closure. *Annual review of genetics,* 48**,** 583-
1064 611.
1065 XU, N., BAGUMIAN, G., GALIANO, M. & MYAT, M. M. 2011. Rho GTPase controls
1066 Drosophila salivary gland lumen size through regulation of the actin cytoskeleton and
1067 Moesin. *Development,* 138**,** 5415-5427.
1068 YAM, C., FUNG, T. & POON, R. 2002. Cyclin A in cell cycle control and cancer. *Cellular and*
1069 *Molecular Life Sciences CMLS,* 59**,** 1317-1326.
1070 YAMAGUCHI, Y., SHINOTSUKA, N., NONOMURA, K., TAKEMOTO, K., KUIDA, K.,
1071 YOSIDA, H. & MIURA, M. 2011. Live imaging of apoptosis in a novel transgenic
1072 mouse highlights its role in neural tube closure. *Journal of Cell Biology,* 195**,** 1047-1060.
1073 ZAMZAMI, N. & KROEMER, G. 1999. Condensed matter in cell death. *Nature,* 401**,** 127-128.
1074 ZIELKE, N., KIM, K. J., TRAN, V., SHIBUTANI, S. T., BRAVO, M.-J., NAGARAJAN, S.,
1075 VAN STRAATEN, M., WOODS, B., VON DASSOW, G. & ROTTIG, C. 2011. Control
1076 of Drosophila endocycles by E2F and CRL4CDT2. *Nature,* 480**,** 123-127.
1077 ZIELKE, N., KORZELIUS, J., VAN STRAATEN, M., BENDER, K., SCHUHKNECHT, G. F.,
1078 DUTTA, D., XIANG, J. & EDGAR, B. A. 2014. Fly-FUCCI: A versatile tool for
1079 studying cell proliferation in complex tissues. *Cell reports,* 7**,** 588-598.

1080

Figure 1-figure supplement 1.

A

***hkb-RA* transcript (1567bp)**

ORF in blue

ZnF domains highlighted (ZnF1, ZnF2, ZnF3)

gRNAs in bold and underlined (gRNA No.3 near the beginning of the ORF; gRNA No.1 in the 2nd ZnF domain)

GCTCAGTTCGAGTCGAGATCTCGCAGCACACACACAGCTCCGCACAACCAAATCAAGTCCAAAATCATAATCACA
AGTGTTCCATCCAAGTGATTTAGTGTCGCGAGAGAGCAATTTAGACCTTCCATTAAAACTACTGCAAAATGTCGA
CGATTAACCTGCATCC**CCCGCAAACCTACTCGCGACTTT**TCCGACCCTGGGATACTCAGCGCCAGGCGGCGAC
CTCGGCGGCACCCAGGACAGTGAAGCAGGAGCCGGAGGCGATTACCATCAAGACGGAGCTGGCCAGCAGCAG
TTTCGGCCACGACTGCGACGGAGACTTCTCCTCCGCATCCTCCTCTGCGTCAAGCAGCAGCAACAGCAGCAAGT
CCTGCTACGAGGAGGCCCTGAACCACAGCAGCTACACCCGCACTTCCACCCCGCTGCTGGACGCCGCCCCGC
ACCCCGTCTTTTCACACCCGCAGTCGTCGCCGTTGGACACGCACGCCGCCGCCACCGCATCCTTGGCTCCGCC
AAACCAGCACGCTCCATTCCTGTCGGCCGCCAGCGATCTCTACTACGCTGCCGCCGCCGCAGCAGCCGCTGCT
GCCTCCACGCCCACTGCCGTCCCGGGCTTCGGCATGGACCCGTTCACTATGGGCCTGATGGAGCAAGAGTACG
CCCGCGTGATGGCCGAGGACGCACAGTTAAAGGCGCTCAACAGCCGCAAGCAGCGGCCGAAGAAGTTCAAGT
GCCCCAACTGCGACGTGGCCTTCTCCAACAACGGCCAGCTGAAGGGCCACATCCGCATCCACACCGGCGAACG
CCCATTTAAGTGCGACGTGAACACATGCGGCAAGACCTTCA**CCCGCAATGAGGAACTGACGCGT**CACAAGCGA
ATCCACACCGGACTGCGGCCGTATCCTTGCAGTGCCTGCGGAAAGAAGTTTGGCCGACGCGACCACTTAAAGA
AGCACATGAAGACGCACATGCCGCAGGAGCGCCAGCTGGGCCCGTCCATCTTCGTGCCCATGTACTCATACCT
TTATGGCTACTGAGAGGGAAATCCTGGCGAGCTTTCCCCTTGCCACGCGACCCTGCATTCCAGCGATCTGTAAA
GCGCTTGCACGCTTTAAACAAGCATTACCGAACCGAATCCAACGAAACGAAACTTAACGCCAGCAAAAACTGCCT
AGCCAATCGTGGACAGAACTACCTCAGCCGTACCTGGCGCAATGTGGCGCACTCACCAAACCCAATCTTTGGAC
CTCGACGATATATGCAAATATTGAGATATTTATTTTTTAACGCGTATTTACACTTCCAGCTACGTGACTGGTTATGA
TATTCGGCACATGTGTAAATAATCCCTAAGTGATCCTTCCTCATATGCTAAGCGATTAAGAAATTTAAGAGATGCC
CGGATTTACGTCTAAGTTATACTAAAGCTGATACTTTAACAGTTTTATAAGCTGATCGTGGTTACCAGATACATAC
GATTTATACACAAAATTATACGATCATGGTTATATCTGAGAGTTGAATTATACGATTTATGTTTACAACACAAAATA
CACAAGAAAAACCG

B

***hkb*^{351} and *hkb*^{391} (gRNA No.3 sequence underlined in the WT sequence)**

WT ATGTCGACGATTAACCTGCATCCCCCGCAAACC TACTCGCGACTTTTCCGACCCTGGGATA
hkb^{351} ATGTCGACGATTAACCTGCATCCCCCGCAAACC T--CTCGCGACTTTTCCGACCCTGGGATA
hkb^{391} ATGTCGACGATTAA----------TCCCTGGGATACTCGCGACTTTTCCGACCCTGGGATA

***hkb*^{121} and *hkb*^{131} (gRNA No.1 sequence underlined in the WT sequence)**

WT ATGCGGCAAG ACCTTCACCCGCAATGAGGAACTGACGCGTCACAAGCGAATC
hkb^{121} ATGCGGCAAG ACCTTCACCCGCA------AGGAACTGACGCGTCACAAGCGAATC
hkb^{131} ATGCGGCAAGGTCT----------GGAACTGACGCGTCACAAGCGAATC

C

WT Hkb protein sequence (297aa; 3 ZnF domains)

MSTINLHPPQTYSRLFRPWDTQRQAATSAAPRTVKQEPEAITIKTELASSSFGHDCDGDFSSASSSASSSSNSSKSCY
EEALNHSSYTRTSTPLLDAAPHPVFSHPQSSPLDTHAAATASLAPPNQHAPFLSAASDLYYAAAAAAAAAASTPTAVP
GFGMDPFTMGLMEQEYARVMAEDAQLKALNSRKQRPKK**FKCPNCDVAFSNNGQLKGHIRIH**TGERP**FKCDVNTCG**
KTFTRNEELTRHKRIHTGLRP**YPCSACGKKFGRRDHLKKHMKTH**MPQERQLGPSIFVPMYSYLYGY

Mutant protein sequence in *hkb*^{121} (296 aa; substitution of N237 & E238 to K237 in the 2nd ZnF domain)

MSTINLHPPQTYSRLFRPWDTQRQAATSAAPRTVKQEPEAITIKTELASSSFGHDCDGDFSSASSSASSSSNSSKSCY
EEALNHSSYTRTSTPLLDAAPHPVFSHPQSSPLDTHAAATASLAPPNQHAPFLSAASDLYYAAAAAAAAAASTPTAVP
GFGMDPFTMGLMEQEYARVMAEDAQLKALNSRKQRPKK**FKCPNCDVAFSNNGQLKGHIRIH**TGERP**FKCDVNTCG**
KTFTRKELTRHKRIHTGLRP**YPCSACGKKFGRRDHLKKHMKTH**MPQERQLGPSIFVPMYSYLYGY

Truncated protein sequence in *hkb*^{131} (235 aa; 1 ZnF domain)

MSTINLHPPQTYSRLFRPWDTQRQAATSAAPRTVKQEPEAITIKTELASSSFGHDCDGDFSSASSSASSSSNSSKSCY
EEALNHSSYTRTSTPLLDAAPHPVFSHPQSSPLDTHAAATASLAPPNQHAPFLSAASDLYYAAAAAAAAAASTPTAVP
GFGMDPFTMGLMEQEYARVMAEDAQLKALNSRKQRPKK**FKCPNCDVAFSNNGQLKGHIRIH**TGERPFKCDVNTCG
KVWN

Truncated protein sequence in *hkb*^{351} (33 aa; no ZnF domains)

MSTINLHPPQTSRDFSDPGILSARRRPRRHPGQ

Mutant protein sequence in *hkb*^{391} (219 aa; No ZnF domains; only the first 5 aa is the same as WT (underlined))

<u>MSTIN</u>PWDTATFPTLGYSAPGGDLGGTQDSEAGAGGDYHQDGAGQQQFRPRLRRRLLLRILLCVKQQQQQQVLLR
GGPEPQQLHPHFHPAAGRRPAPRLFTPAVVAVGHARRRHRILGSAKPARSIPVGRQRSLLRCRRRSSRCCLHAHCR
PGLRHGPVHYGPDGARVRPRDGRGRTVKGAQQPQAAAEEVQVPQLRRGLLQQRPAEGPHPHPHRRTPI

Figure 1-figure supplement 1. Indels of the CRISPR/Cas9 *hkb* alleles and predicted protein sequences for each allele. (A) The nucleotide sequence of the *hkb-RA* transcript. The open reading frame (ORF) is marked in blue. Three ZnF domains are highlighted in green (ZnF1), yellow (ZnF2), and magenta (ZnF3), respectively. Two gRNA sequences used to create *hkb* alleles are indicated in bold and underlined. (B) CRISPR/Cas9-induced indels in *hkb* mutants. Nucleotides deleted and inserted in each mutant are indicated by dashed lines and red letters, respectively. (C) Sequences of the WT Hkb protein and predicted proteins in each *hkb* mutant.

Figure 1-figure supplement 2

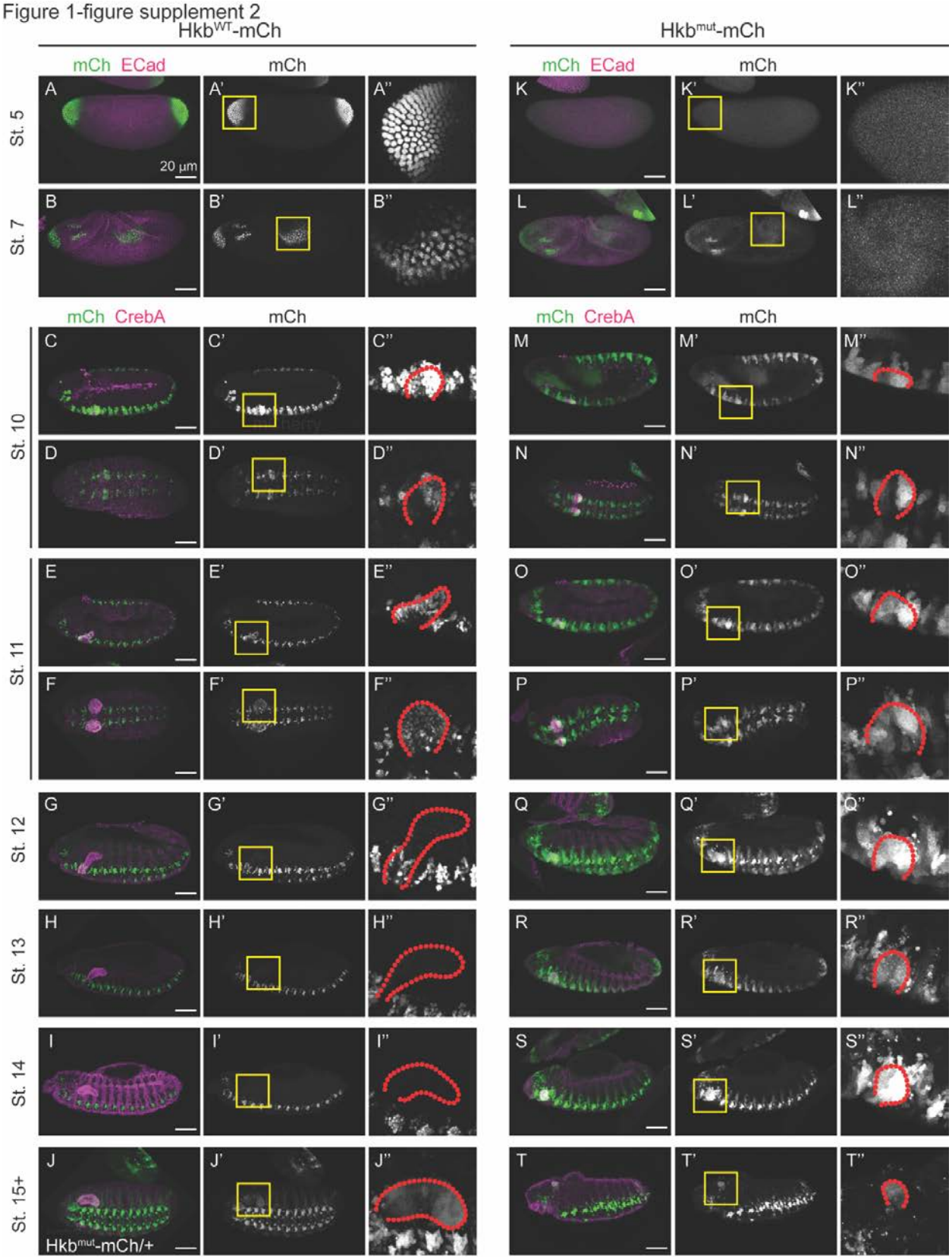

Figure 1-figure supplement 2. Hkb^{wt}-mCh and Hkb^{mut}-mCh signals during embryonic development. (A-T'') Hkb^{wt}-mCh (A-I'') and Hkb^{mut}-mCh (J-T'') expression patterns in embryos at different stages. Yellow boxed regions in A'-T' are shown in higher magnification in A''-T''. SGs are outlined by red dotted lines in M''-T''. (A-A'') At stage 5, Hkb^{wt}-mCh signals localize to the nuclei of the cells at the anterior and posterior poles of the embryo. (B-B'') At stage 7, Hkb^{wt}-mCh signals are seen in the nuclei of the anterior region and in the posterior midgut of the embryo. (C-D'') At stage 10, strong nuclear Hkb^{wt}-mCh signals are seen along the CNS and in the posterior region of the SG of the embryo. mCherry signals localize to the nuclei of the cells. (C-C'') Lateral view. (D-D'') Dorsal view. (E-F'') At stage 11, strong nuclear Hkb^{wt}-mCh signals are seen in all SG cells. (G-G'') At stage 12, Hkb^{wt}-mCh signals are significantly reduced in SG nuclei, while mCh signals are consistently high in CNS cells. (H-H'') At stage 13, very low levels of Hkb^{wt}-mCh signals are seen in SG nuclei. (I-I'') At stage 14, Hkb^{wt}-mCh signals of SG nuclei are reduced to almost undetectable levels. (J-T'') Hkb^{mut}-Ch signals are seen throughout the cell. (J-J'') mCh signals in Hkb^{mut}-mCh/+ heterozygous embryo at stage 16. mCh signals persist in the SG. (M-T'') mCh signals in Hkb^{mut}-mCh homozygous embryos. mCh signals persist in the SG throughout embryogenesis and are seen throughout the cell.

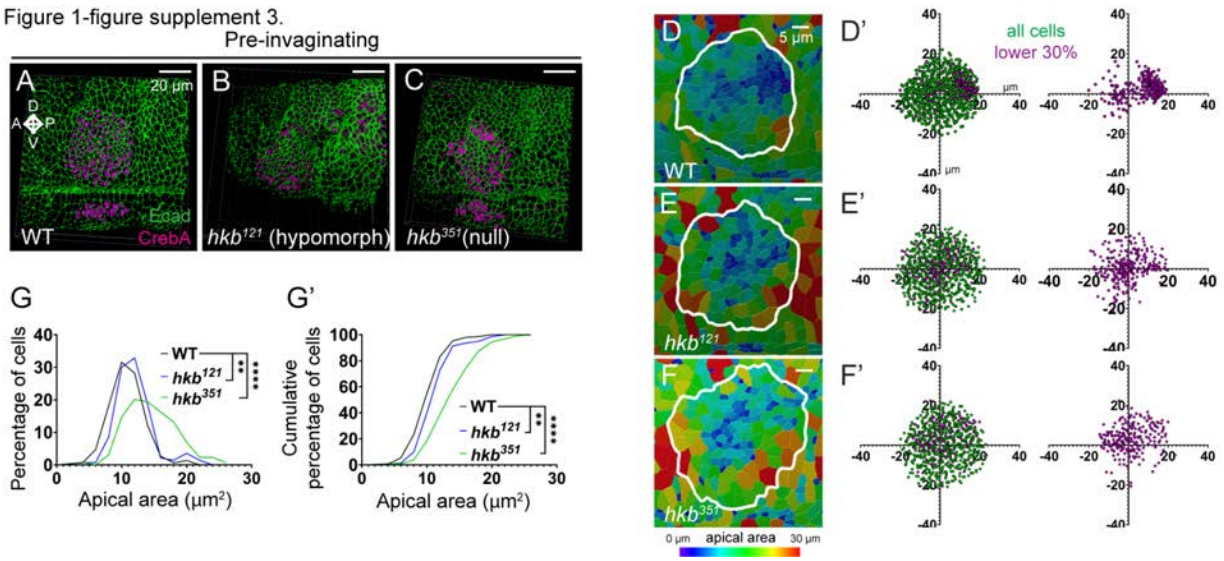

Figure 1-figure supplement 3. Quantification of apical areas in the pre-invaginating SG of WT and *hkb* mutant embryos. (A-C) Three-dimensional reconstruction of confocal images of pre-invaginating SGs immunolabeled with Ecad and CrebA. (D-F) Heat maps of apical area distribution in pre-invaginating SGs. (D'-F') Scatter plots showing the relative position of total SG cells (green) and cells with small apical areas (magenta). The X and Y axes represent the distance along the A/P and D/V axes, respectively, from the center of the placode. Cells in the bottom 30% of the apical area (magenta) and all cells (green) are plotted. N=7 SGs (WT, 932 cells; hkb^{121}, 727 cells; hkb^{351}, 864 cells) (G, G') Quantification of apical area distribution in SG cells before invagination. Mann-Whitney U test (percentage of cells) and Kolmogorov-Smirnov test (cumulative percentage of cells). **, $p<0.01$; ****, $p<0.0001$.

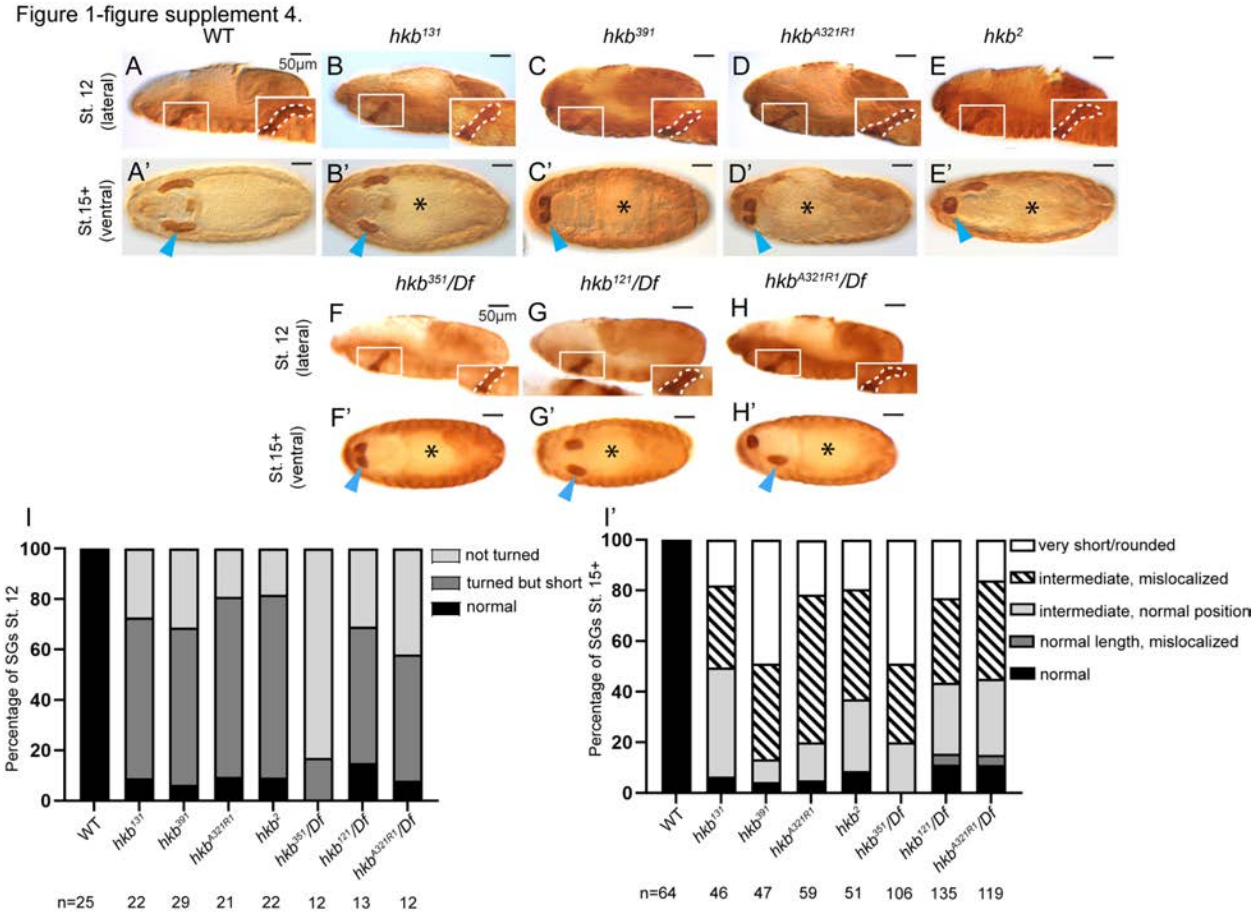

Figure 1-figure supplement 4. SG phenotypes in different *hkb* alleles. (A-H') Stage 12 (A-E; lateral) and stage 15+ (A'-H'; ventral) embryos immunostained for CrebA. The insets show a magnified view of the region in the white rectangles, with the SG outlined by white dashed lines. Cyan arrowheads, SGs in stage 15+ embryos. Asterisks, defective gut morphology. (I, I') Quantification of the SG phenotypic distribution at stage 12 (I) and stage 15 (I'). The number of embryos used is indicated below each genotype. Statistical significance was calculated by two-way ANOVA. $p<0.05$.

Figure 1-figure supplement 5.

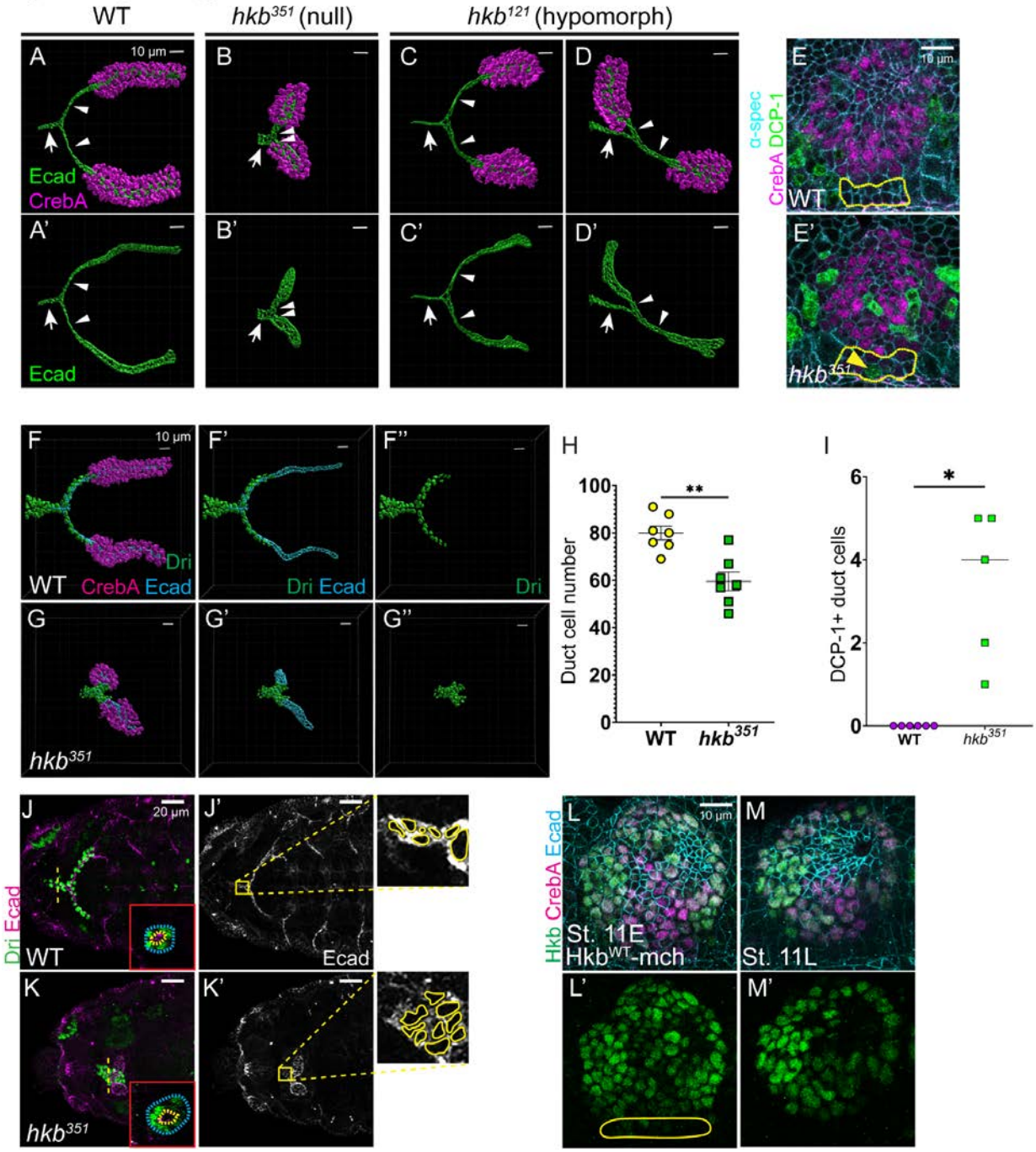

Figure 1-figure supplement 5. *hkb* mutants show short salivary duct phenotypes with reduced cell numbers and cell intercalation defects. (A-D') 3D reconstruction of the confocal images of stage 15+ SGs immunolabeled with Ecad (green) and CrebA (magenta). Arrows, common duct. Arrowheads, individual duct. (E-E') Confocal images of stage 11 SGs immunolabeled with α-spectrin (cyan; lateral membrane), CrebA (magenta), and DCP-1 (green).

Yellow dotted lines, SG duct cells. Yellow arrowhead, DCP-1-positive duct cell. (F-G'') 3D reconstruction of the confocal images of stage 15+ SGs immunolabeled with Dri (green), CrebA (magenta), and Ecad (cyan). (H) Quantification of ductal cell number. N=7. Statistical significance was calculated by Student's t-test. **, $p<0.01$. (I) Quantification of DCP-1-positive duct cells. N=6 (WT); 5 (*hkb*^{351}). Statistical significance was calculated by Student's t-test. *, $p<0.05$. (J-K') Confocal images of SGs immunolabeled with Ecad (magenta) and Dri (green). Z-sections along the yellow dashed lines in H and I are shown as insets. Yellow boxed regions in H' and I' are shown at higher magnification, with the boundary of each salivary duct cell marked with yellow lines. (L-M') Confocal images of SGs immunolabeled with mCh (green), CrebA (magenta), and Ecad (Cyan). Yellow line, duct cells.

Figure 2-figure supplement 1.

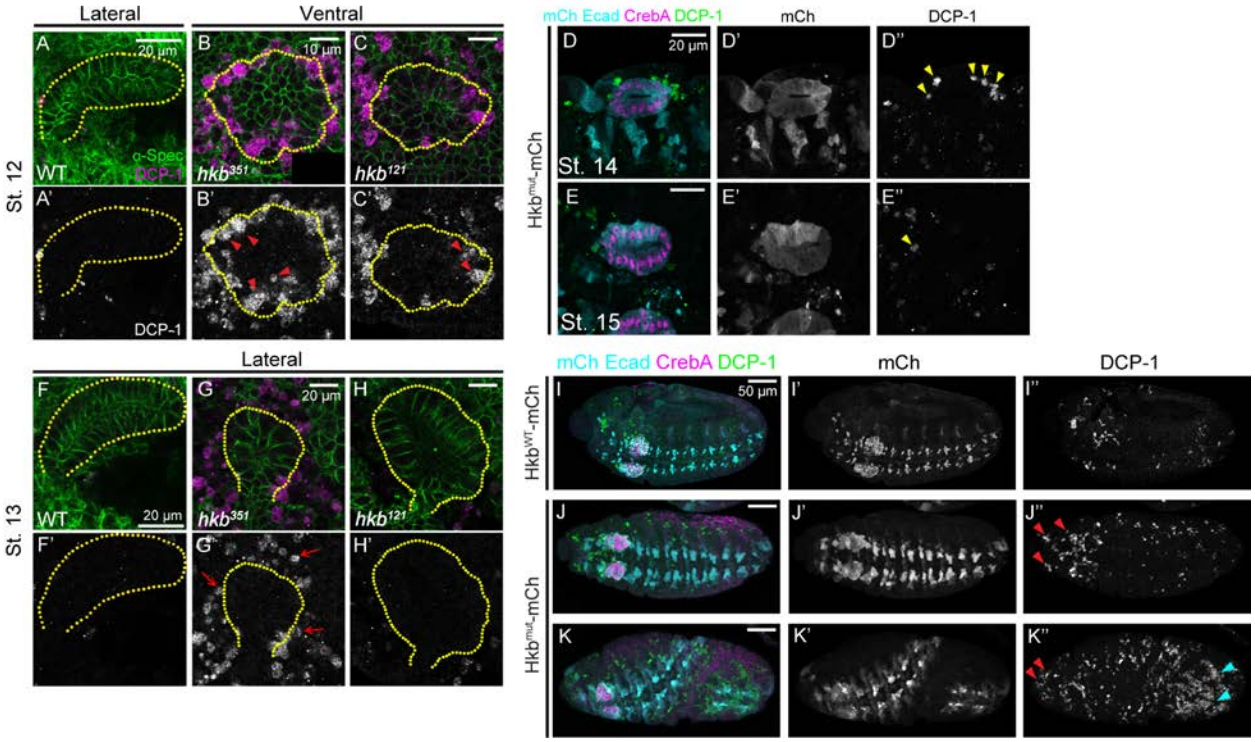

Figure 2-figure supplement 1. DCP-1 signals in late stage SGs and other regions of *hkb* mutant embryos. (A-C') Confocal images of SGs in stage 12 WT and *hkb* mutant embryos immunostained for α-Spec (green) and DCP-1 (magenta). Yellow dotted lines, SG boundary. Arrowheads in B' and C', DCP-1 signals in the cells within the SG placode. (D-E'') Confocal images of SGs in stage 14 and 15 Hkb^{mut}-mCh embryos stained for mCh and Ecad (cyan), CrebA (magenta), and DCP-1 (green). Arrows in J'', DCP-1-positive cells near the SG at stage 14. (F-H') Confocal images of SGs in stage 13 WT and *hkb* mutants immunostained for α-Spec (green) and DCP-1 (magenta). Yellow dotted lines, SG boundary. Arrows in G', DCP-1 signals near the SG placode. (I-K'') Confocal images of stage 11 embryos immunostained for Ecad and mCh (cyan), CrebA (magenta), and DCP-1 (green). Hkb^{mut}-mCh embryos show increased DCP-1 signals in other regions of the embryo compared to Hkb^{WT}-mCh embryos, with a greater increase in the head region (red arrowheads) and posterior region (cyan arrowheads in I'').

Figure 2-figure supplement 2.

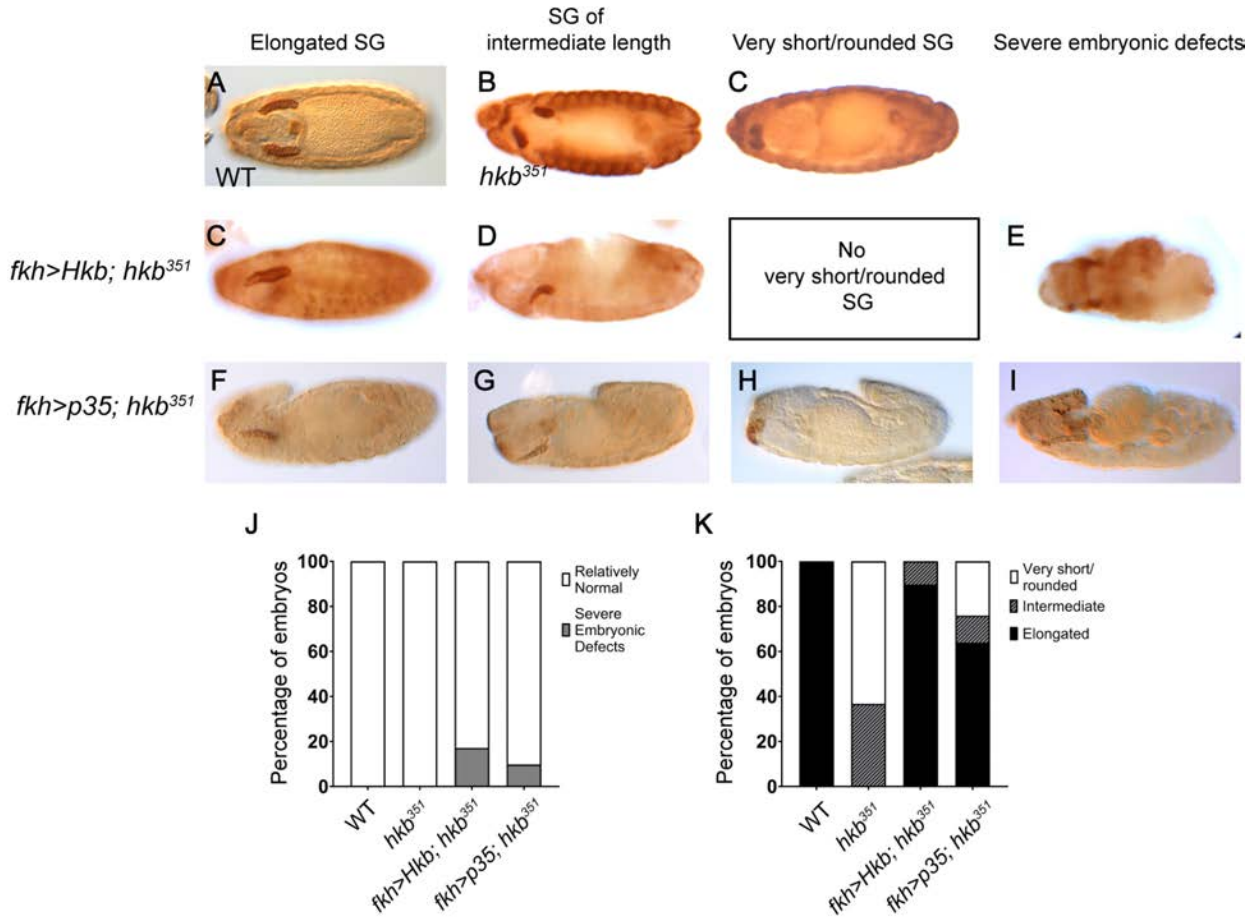

Figure 2-figure supplement 2. Overexpression of Hkb or p35 rescues *hkb* mutant SG phenotypes. (A-I) Embryos stained for CrebA. WT (A), *hkb* mutant (B, C), overexpression of Hkb (C-E) or p35 (F-I) in the SG using the *fkh-Gal4* driver in the *hkb* mutant background results in a range of the phenotypes consisting mostly of fully elongated SGs as in WT (C, F), some SGs of intermediate length (D, G), and a few SGs with a very short/rounded phenotype as in *hkb* null mutants (H). Some embryos also show severe morphological defects (E, I). (J-K) Quantification of embryonic (J) and SG (K) morphology. N=25 (WT), 30 (hkb^{351}), 29 (*fkh>Hkb*; hkb^{351}), 92 (*fkh>p35*; hkb^{351}).

Figure 2-figure supplement 3.

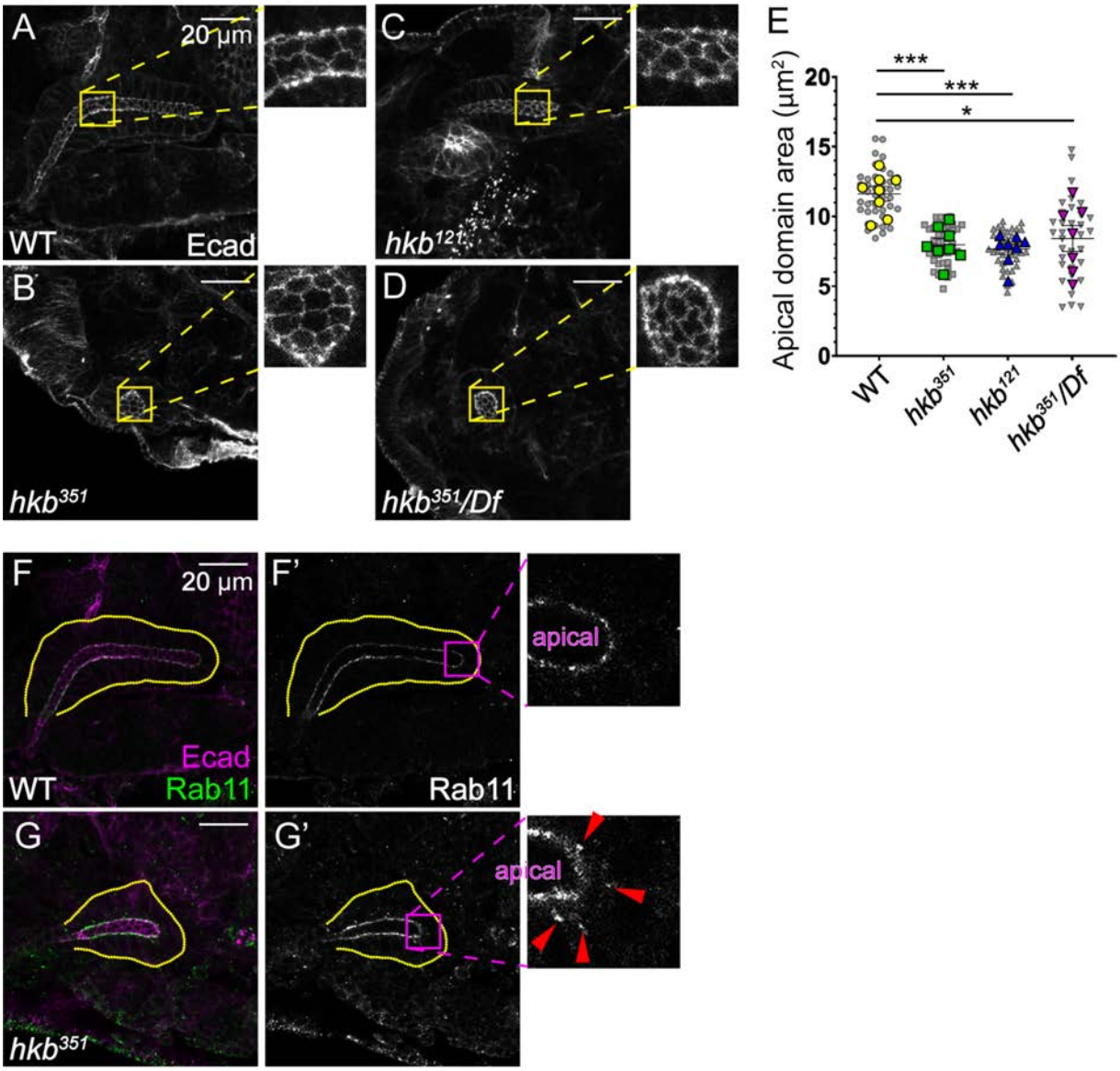

Figure 2-figure supplement 3. *hkb* mutant SGs have a smaller apical domain size with Rab11 mislocalized to the basolateral domain. (A-D) Confocal images of SGs in stage 15 embryos immunostained for Ecad. Apical domains in the yellow boxed regions are shown at higher magnification. (E) Quantification of the apical area of individual SG cells. (F, G) Confocal images of SGs in stage 15 embryos immunostained for Rab11. Magenta boxed regions are shown at higher magnification. Yellow dotted lines, basal boundary of the SG. Red arrowheads, small punctate Rab11 signals often observed in the basolateral region of SG cells in *hkb* mutants.

Figure 5-figure supplement 1.

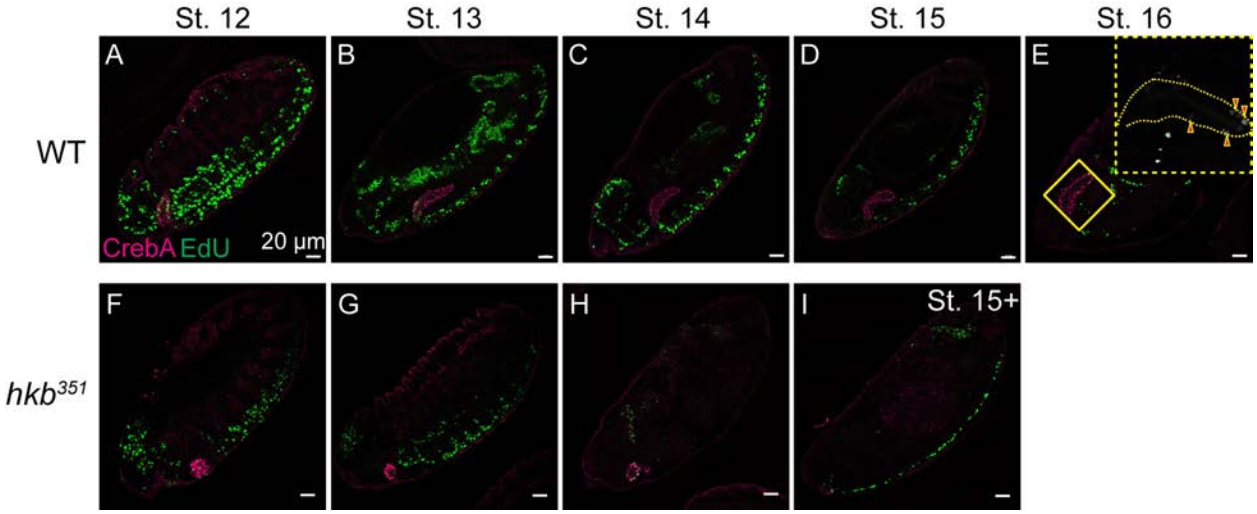

Figure 5-figure supplement 1. EdU signals during mid to late embryogenesis in WT and *hkb* mutant embryos. (A-I) Confocal images of WT (A-E) and *hkb* mutant (F-I) embryos pulsed and labeled for EdU (green) and immunolabeled for CrebA (magenta). Insets, higher magnification images for the regions highlighted with the yellow boxes. Arrowheads, cells with EdU signals.

Figure 6-figure supplement 1

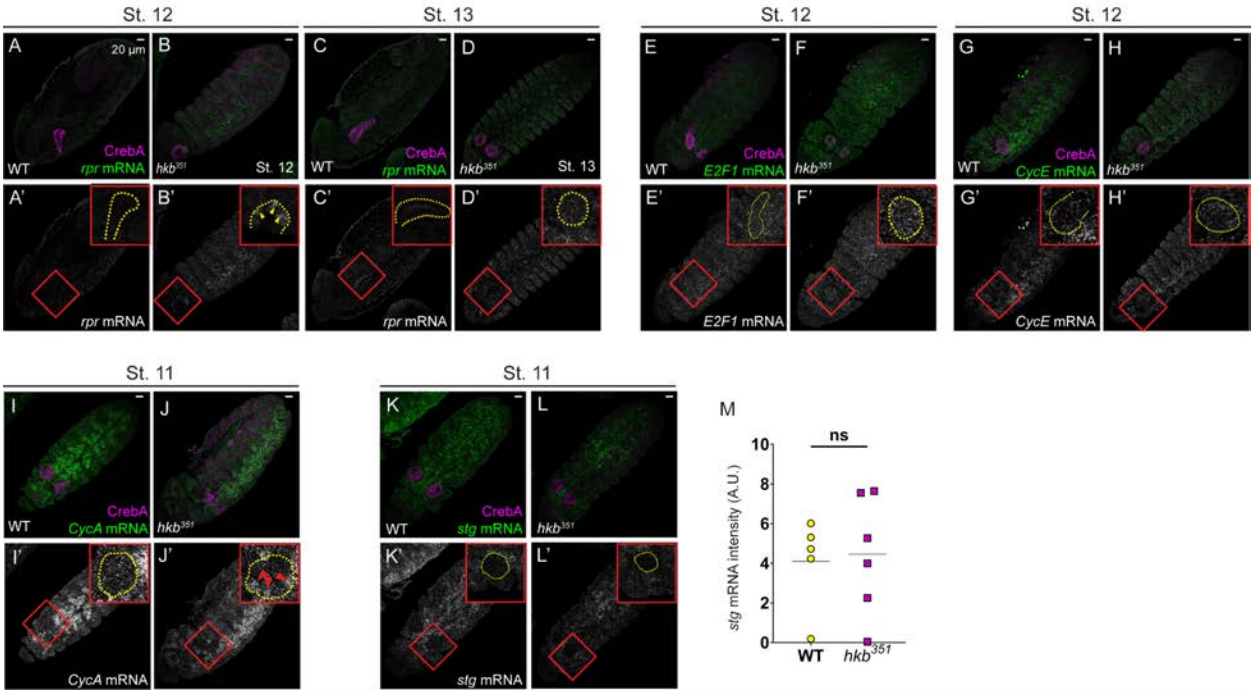

Figure 6-figure supplement 1. Expression levels of key cell cycle and cell death genes. (A-L') Confocal images of embryos from fluorescence *in situ* hybridization experiment showing mRNA levels of *rpr* at stage 12-13 (A-D'), *E2f1* at stage 12 (E-F'), *CycE* at stage 12 (G-H'), *CycA* at stage 11 (I-J'), and *stg* at stage 11 of embryogenesis (K-L'). (A-D') At stage 12, compared to the ubiquitously low level of *rpr* in WT SGs, a few SG cells maintain high levels of *rpr* (yellow arrowheads). At stage 13, *rpr* transcript levels are very low in the SG of both genotypes. (E-F') In WT SGs, *E2F1* mRNA shows basal levels comparable to neighboring cells. In *hkb* mutant SGs, *E2F1* transcript levels are slightly higher than in neighboring cells. (G-H') In WT SGs, *CycE* levels are not significantly higher than the neighboring cells at stage 12, and in *hkb* mutant SGs, *CycE* mRNA levels are slightly elevated and comparable to neighboring cells. (I-J') In WT SGs, *CycA* shows placode-wide underexpression. In *hkb* mutants, *CycA* mRNA levels are significantly elevated in some SG cells (red arrowheads). (K-L') Compared to most ventral epidermal tissues, *stg* is downregulated in both WT and *hkb* mutant SGs at stage 11. (M) Quantification of *stg* levels in WT and *hkb* mutant SGs. N=5 (WT), 6 (hkb^{351}). Statistical analysis was performed using Student's t-test with Welch's correction. Red boxes indicate the

SG regions at higher magnification shown as insets in A’-L’. Yellow dotted lines indicate the SG boundary.

Figure 6-figure supplement 2.

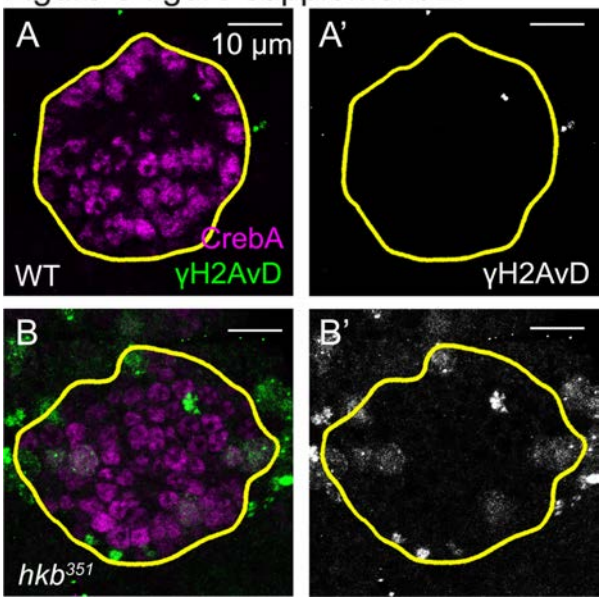

Figure 6-figure supplement 2. γ-H2Av signals are increased in *hkb* mutant SGs at stage 11. (A-B') Confocal images of SGs in WT (A-A') and *hkb* mutant (B-B') embryos immunostained for CrebA (magenta) and γ-H2Av (green). *hkb* mutant SGs show an increase in γ-H2Av signals in the entire placode compared to WT. Yellow lines, SG boundary.

Figure 6-figure supplement 3

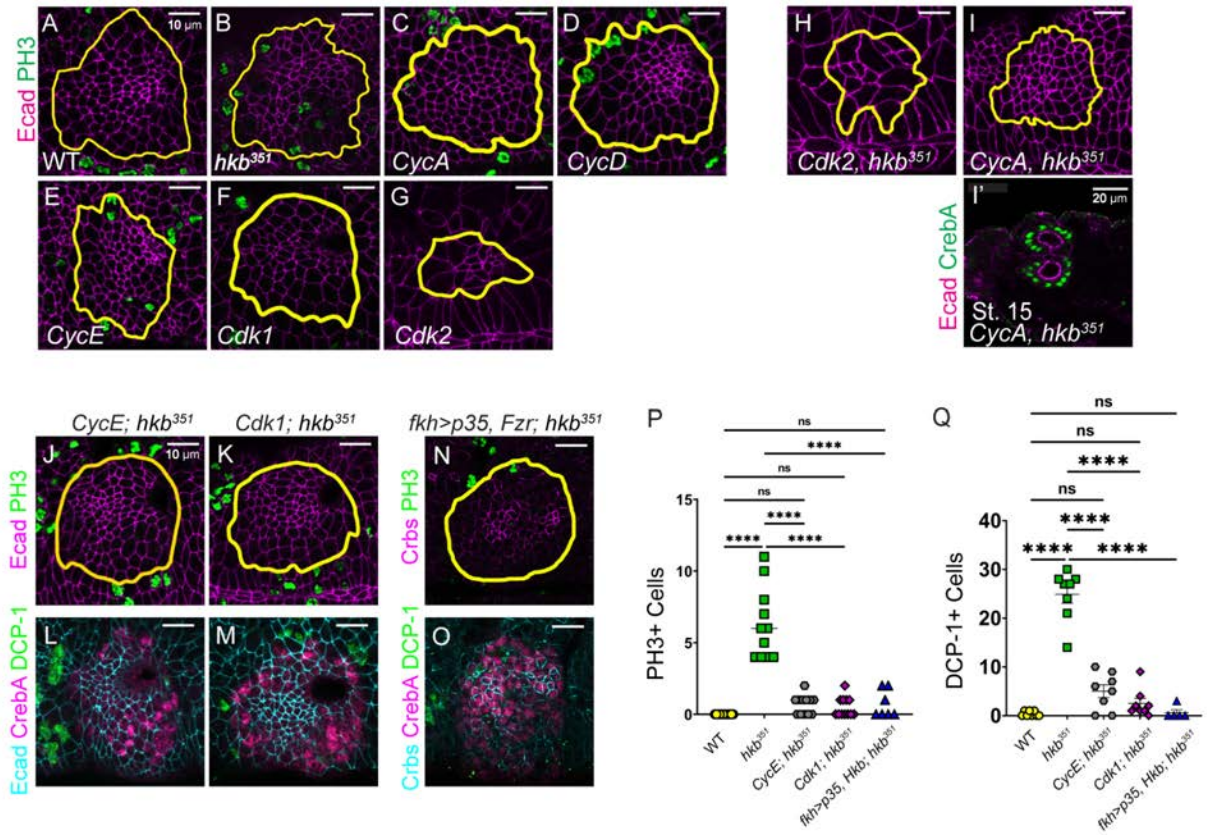

Figure 6-figure supplement 3. Genetic inhibition of the function of key cell cycle genes is sufficient to suppress cell death and cell division in *hkb* mutants. (A-G) SGs in stage 11 embryos of WT and mutants for *hkb* and several key cell cycle genes, immunostained for Ecad (magenta) and PH3 (green). Single mutants for *CycA*, *CycD*, *CycE*, and *Cdk1* have relatively normal SG morphology, with few SG cells expressing PH3 (green) in *CycD* and *CycE* mutants. *Cdk2* mutant embryos have severe morphological defects, including significantly fewer SG cells. (H-I') SGs in stage 11 embryos double mutant for *Cdk2* and *hkb* (H) and *CycA* and *hkb* (I-I'). *Cdk2 hkb* double mutant embryos show severe morphological defects similar to *Cdk2* single mutant embryos, with significantly reduced SG cell numbers. *CycA hkb* double mutants show the same range of phenotypes as *hkb* mutants, including the centralized invagination phenotype and small SG at later embryonic stages. (J-O) Confocal images of SGs at stage 11 embryos double mutant for *CycE* and *hkb* (J, L), *Cdk1* and *hkb* (K, M), or overexpression of p35 and Fzr in the *hkb* mutant SG using the fkh-Gal4 driver (N, O). (J, K, N) Embryos immunostained for PH3 (green), Ecad (J, K; magenta) or Crb (N; magenta). (L, M, O) Embryos are immunostained for

CrebA (magenta), DCP-1 (green), and Ecad (L, M; cyan) or Crumbs (O; cyan). (P-Q) Quantification of the number of PH3-positive (P) and DCP-1-positive SG cells (Q) at stage 11. (P) N= 12 SGs for all genotypes except for *fkh>p35, Fzr; hkb*^{351} (7 SGs). (Q) N=8 SGs (for all genotypes except for *fkh>p35, Fzr; hkb*^{351} (6 SGs). Statistical significance was calculated using a one-way ANOVA test with multiple comparisons. ****, $p<0.0001$.

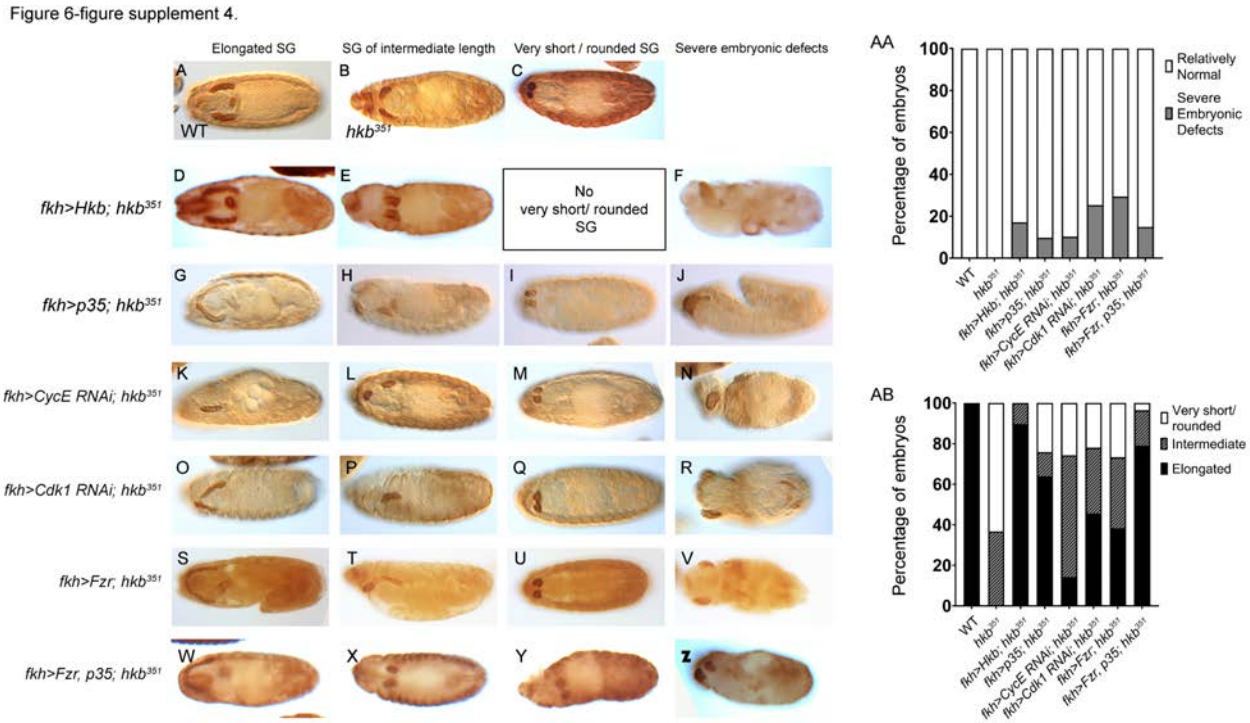

Figure 6-figure supplement 4. Inhibition of cell division or cell death partially rescues the SG phenotypes of *hkb* mutants. (A-Z) Embryos stained for CrebA. Overexpression of Hkb (D-F) or p35 (G-J) as well as knockdown of *CycE* (K-N), *Cdk1* (O-R), overexpression of Fzr (S-V), or overexpression of both Fzr and p35 (W-Z) in *hkb* mutant SGs using the *fkh-Gal4* driver results in a range of rescue effects, including fully elongated SGs as in WT (A, D, G, K, O, S, W), SGs of intermediate length (B, E, H, L, P, T, X), SGs with a very short/rounded phenotype as in *hkb* null mutants (C, I, M, Q, U, Y). Some embryos also show severe morphological defects (F, J, N, R, V, Z). (AB) Quantification of SG morphology. Embryos with normal morphology (AB) as shown in A-C, D-E, G-I, K-M, O-Q, S-U, and W-Y were used for quantification. Note that the quantification for WT, hkb^{351}, *fkh>Hkb*; hkb^{351}, and *fkh>p35*; hkb^{351} is the same as shown in Figure 2-figure supplement 2. N=25 (WT), 30 (hkb^{351}), 29 (*fkh>Hkb*; hkb^{351}), 92 (*fkh>p35*; hkb^{351}), 68 (*fkh>Cdk1RNAi*; hkb^{351}), 35 (*fkh>CycERNAi*; hkb^{351}), and 60 (*fkh>Fzr;* hkb^{351}), and 86 (*fkh>p35, Fzr;* hkb^{351}) embryos. Statistical significance was calculated by two-way ANOVA.